RESEARCH ARTICLE

Special Section:
Fire in the Earth System

Key Points:
- NO$_x$ and HONO are rapidly converted to other species. The average *e*-folding time (distance) for NO$_x$ is ~90 min (~40 km)
- In 4 h, PANs contribute ~37% of the ΣNO$_y$ species in smoke; *p*NO$_3$ is the second largest (~27%) contributor
- In 4 h, Org N$_{(g)}$ constitute a large portion (~23%) of the ΣNO$_y$ in the plumes sample during WE-CAN

Supporting Information:
- Supporting Information S1

Correspondence to:
J. F. Juncosa Calahorrano and E. V. Fischer
jjuncosa@colostate.edu;
evf@rams.colostate.edu

Daytime Oxidized Reactive Nitrogen Partitioning in Western U.S. Wildfire Smoke Plumes

Julieta F. Juncosa Calahorrano[1], Jakob Lindaas[1], Katelyn O'Dell[1], Brett B. Palm[2], Qiaoyun Peng[2], Frank Flocke[3], Ilana B. Pollack[1], Lauren A. Garofalo[4], Delphine K. Farmer[4], Jeffrey R. Pierce[1], Jeffrey L. Collett Jr.[1], Andrew Weinheimer[3], Teresa Campos[3], Rebecca S. Hornbrook[3], Samuel R. Hall[3], Kirk Ullmann[3], Matson A. Pothier[4], Eric C. Apel[3], Wade Permar[5], Lu Hu[5], Alan J. Hills[3], Deedee Montzka[3], Geoff Tyndall[3], Joel A. Thornton[4], and Emily V. Fischer[1]

[1]Department of Atmospheric Science, Colorado State University, Fort Collins, CO, USA, [2]Department of Atmospheric Sciences, University of Washington, Seattle, WA, USA, [3]Atmospheric Chemistry Observations & Modeling Laboratory, National Center for Atmospheric Research, Boulder, CO, USA, [4]Department of Chemistry, Colorado State University, Fort Collins, CO, USA, [5]Department of Chemistry and Biochemistry, University of Montana, Missoula, MT, USA

Abstract The Western Wildfire Experiment for Cloud Chemistry, Aerosol Absorption, and Nitrogen (WE-CAN) deployed the NSF/NCAR C-130 aircraft in summer 2018 across the western U.S. to sample wildfire smoke during its first days of atmospheric evolution. We present a summary of a subset of reactive oxidized nitrogen species (NO$_y$) in plumes sampled in a pseudo-Lagrangian fashion. Emissions of nitrogen oxides (NO$_x$ = NO + NO$_2$) and nitrous acid (HONO) are rapidly converted to more oxidized forms. Within 4 h, ~86% of the ΣNO$_y$ is in the form of peroxy acyl nitrates (PANs) (~37%), particulate nitrate (*p*NO$_3$) (~27%), and gas-phase organic nitrates (Org N$_{(g)}$) (~23%). The average *e*-folding time and distance for NO$_x$ are ~90 min and ~40 km, respectively. Nearly no enhancements in nitric acid (HNO$_3$) were observed in plumes sampled in a pseudo-Lagrangian fashion, implying HNO$_3$-limited ammonium nitrate (NH$_4$NO$_3$) formation, with one notable exception that we highlight as a case study. We also summarize the observed partitioning of NO$_y$ in all the smoke samples intercepted during WE-CAN. In smoke samples intercepted above 3 km above sea level (ASL), the contributions of PANs and *p*NO$_3$ to ΣNO$_y$ increase with altitude. WE-CAN also sampled smoke from multiple fires mixed with anthropogenic emissions over the California Central Valley. We distinguish samples where anthropogenic NO$_x$ emissions appear to lead to an increase in NO$_x$ abundances by a factor of four and contribute to additional PAN formation.

1. Introduction

Biomass burning directly impacts air quality, nutrient cycles, weather, and climate by releasing large amounts of trace gases and particulate matter into the atmosphere (Akagi et al., 2011; Bond et al., 2004; Crutzen & Andreae, 1990; Fearnside et al., 1993). Because western U.S. wildfire activity is expected to increase in a drier and warmer climate (Hudman et al., 2004; Keywood et al., 2013; Moritz et al., 2012; Scholze et al., 2006; Westerling, 2016; Williams et al., 2019; Yue et al., 2013), it is vital to understand the impacts of smoke on atmospheric composition on local and regional scales. Here we focus on the evolution of oxidized nitrogen in western U.S. wildfire smoke plumes. Understanding the near-source first hours of evolution of the oxidized nitrogen in smoke is necessary to predict its further partitioning (i.e., species, phase, amount) as plumes age (Akagi et al., 2012; Liu et al., 2016). The partitioning and evolution of the oxidized nitrogen emitted from fires influences the production of free radicals (Peng et al., 2020) and oxidants in wildfire plumes, which in turn drives the formation and removal of secondary pollutants (e.g., Akagi et al., 2012; Alvarado et al., 2010; Liu et al., 2016; R J. Yokelson et al., 2009). Moreover, longer-lived non-radical reservoir species such as peroxy acyl nitrates (PANs) can travel long distances impacting air composition on regional and global scales (e.g., Val Martin et al., 2006).

Prior field, laboratory, and modeling experiments provide strong foundational knowledge of the emissions and evolution of oxidized nitrogen emissions from biomass burning. During biomass burning, nitrogen in the fuel is released into the atmosphere (Kuhlbusch et al., 1991; Lobert et al., 1990). Different forms of nitrogen are emitted or formed during different processes. Small nitrogen-containing molecules (e.g., hy-

drogen cyanide (HCN), ammonia (NH_3), and isocyanic acid (HNCO)) are typically emitted during pyrolysis (Glarborg et al., 2018; Hansson et al., 2004; Roberts et al., 2020). Radical chemistry within flames converts a fraction of these species to more oxidized forms including N_2, nitrous oxide (N_2O), nitrogen oxide (NO), nitrogen dioxide (NO_2), and nitrous acid (HONO) (Ren & Zhao, 2012; Scharko et al., 2019). The most abundant emitted reactive N species include nitrogen oxides ($NO_x = NO + NO_2$), NH_3, nitrous acid (HONO), HCN, and acetonitrile (CH_3CN) (e.g., Akagi et al., 2011; Andreae, 2019; Andreae & Merlet, 2001). Prior to the Fire Influence on Regional and Global Experiment (FIREX) Fire Lab 2016 experiments, laboratory, and field studies have shown that for a given fuel, emissions of reduced forms of nitrogen (e.g., NH_3) are favored during smoldering conditions, whereas oxidized forms of nitrogen (e.g., NO, NO_2) are favored during flaming conditions (Burling et al., 2010; Goode et al., 2000; McMeeking et al., 2009; Robert J. Yokelson et al., 1996). In recent work, Roberts et al. (2020) find high- and low-temperature pyrolysis to also be important factors driving the emissions for certain reactive nitrogen species.

The species and phase of oxidized nitrogen in smoke plumes are rapidly processed chemically within minutes to hours after emission. For example, observations of smoke from deforestation and crop residue fires in the Yucatan Peninsula (R J. Yokelson et al., 2009), boreal fires (Alvarado et al., 2010), and chaparral fires in California (Akagi et al., 2012) suggest fast conversion (within 1–2 h) of NO_x into more oxidized forms such as peroxyacetyl nitrate (PAN) and other nitrates. Liu et al. (2016) report on emissions and the first hour of the evolution of trace gases from 15 agricultural fires in the southeast U.S. They observed fast PAN and aerosol nitrate production and little to no gas-phase nitric acid (HNO_3) enhancement in the plumes. These observations suggest that PAN and aerosol nitrate comprise a large portion of the total NO_y in smoke plumes that are more than a few hours old. In addition, Briggs et al. (2017) report that in aged smoke plumes (i.e., 1–2 days) observed over the U.S. Pacific Northwest, NO_x, PAN, and aerosol nitrate comprise on average 11%, 36%, and 51%, respectively, of the observed total NO_y. While many past field campaigns have quantified NO_x, PANs, and aerosol nitrate in smoke, observations of many of the other oxidized species including multifunctional organic nitrates, and peroxy nitrates are new. In contrast to the work we present here, their overall contribution is often inferred from measurements of total NO_y. Here we present a "bottom up" accounting of NO_y which includes the most abundant oxidized reactive nitrogen species measured during WE-CAN. In this study, ΣNO_y refers to the sum of NO, NO_2, PAN, peroxypropionyl nitrate (PPN), HONO, HNO_3, pNO_3, oxidized nitrogen-containing volatile organic compounds (NVOC), and Org $N_{(g)}$.

A more limited body of existing research also provides several insights into oxidized nitrogen chemistry in situations where smoke from western U.S. wildfires mixes with urban emissions. J. Lindaas et al. (2017) report on aged smoke (i.e., 2–3 days) from the Pacific Northwest and Canada impacting the urban Colorado Front Range. They observed several perturbations to the local NO_y budget, including PAN and PPN enhancements of ~100% above background concentrations as well as shifts in the peak of the diurnal cycle of PAN to later in the day during the smoke-impacted periods. Similar to PAN and PPN, lower-mass alkyl nitrate molecules (C_1–C_2) showed enhancements (41% and 31% for methyl and ethyl nitrate, respectively) while the higher-mass alkyl nitrate molecules (C_3–C_5) showed shifts to later in the day in their diurnal cycle peaks. NO_2 was enhanced compared to smoke-free time periods near sunrise and sunset, probably driven by a change in the $NO:NO_2$ ratio. H. B. Singh et al. (2012) used aircraft observations of smoke mixed with urban emissions from the Arctic Research of the Composition of the Troposphere from Aircraft and Satellites— California Air Resource Board (ARCTAS-CARB) campaign to challenge a regional air quality model (Community Multi-scale Air Quality [CMAQ] regional model). The model substantially underpredicted observations of secondary pollutants (ozone [O_3], PAN, and formaldehyde [HCHO]). Similarly, Cai et al. (2016) used the observations from the ARCTAS-CARB campaign to evaluate the predictions of a fine-resolution regional air quality modeling system (CMAQ). The model results predicted the total NO_y mixing ratios; however, larger uncertainties were found in the partitioning between individual NO_y compounds. The available literature (e.g., Akagi et al., 2013; Cai et al., 2016; Selimovic et al., 2020; H. B. Singh et al., 2012) shows that when smoke-impacted air masses mix with urban emissions, there is additional chemistry that might not be represented in air quality models. Air quality models require improvements to emission estimates, chemical mechanisms (including more detailed photochemistry), plume injection height, and meteorological inputs, to improve the results on nitrogen chemistry in smoke-impacted air masses (Cai et al., 2016).

The Western Wildfire Experiment for Cloud Chemistry, Aerosol Absorption, and Nitrogen (WE-CAN) field campaign provides an opportunity to examine the partitioning of oxidized reactive nitrogen across a variety of western U.S. wildfire smoke plumes. During the summer 2018 fire season, an instrumented National Science Foundation/National Center for Atmospheric Research (NSF/NCAR) C-130 research aircraft systematically sampled the emissions and near-field (<215 km from the centroid of the active burn area) evolution of >20 western U.S. wildfire plumes. The aircraft payload consisted of a large suite of instrumentation for the measurement of major anticipated NO_y species. The aircraft also intercepted numerous smoke plumes from additional wildfires across the western U.S. Given the number of smoke plumes sampled, the large number of different chemical measurements, and the complex/diverse chemistry governing different processes relevant to the partitioning of N, there are several dovetailing manuscripts based on the WE-CAN dataset. Peng et al. (2020) document the emissions and evolution of HONO in fresh smoke plumes sampled during WE-CAN. Lindaas et al. (2020) describe the emissions of all the N-compounds measured during WE-CAN. Lindaas et al. (under review) discuss the evolution of reduced nitrogen (i.e., NH_3 and pNO_4) in the fresh plumes sampled during WE-CAN.

The current paper is tightly focused on a comprehensive summary of the observed evolution of oxidized nitrogen species across all the smoke plumes sampled during WE-CAN. First, we summarize the evolution of the most abundant oxidized nitrogen species (ΣNO_y) across 17 fresh smoke plumes with physical ages ranging from ~1 to ~6 h. We then provide case studies of two particularly well-sampled smoke plumes and discuss observed differences in ΣNO_y partitioning between these fires. We also summarize ΣNO_y partitioning across all the smoke samples intercepted during WE-CAN as a function of altitude and relative chemical age. Finally, we compare observations of smoke mixed with urban emissions from the California Central Valley with prior observations of this interaction in this region. Future papers, currently in progress, investigate the chemical mechanisms supporting PAN and O_3 production in the WE-CAN wildfire smoke plumes using the in situ observations alongside models. Thus, these latter topics are not included here.

2. Methods

2.1. Overview of WE-CAN Flights and Sampling Strategy

In summer 2018, WE-CAN deployed the NSF/NCAR C-130 to answer questions related to the evolution of reactive nitrogen emitted from wildfires, cloud-smoke interactions, and absorbing aerosols (https://www.eol.ucar.edu/field_projects/we-can). There were a total of 16 research flights (RF) based out of Boize, ID and 3 educational flights (EF) based out of Broomfield, CO. WE-CAN sampled smoke plumes from 23 fires with identified locations, as well as smoke-impacted air masses, and cloud-smoke mixtures. The sampling strategy for smoke plumes from fires with identified locations normally began by characterizing the background air upwind of the fire source. From here the aircraft traversed the smoke plumes downwind of the fire source. The aircraft crossed plumes perpendicular to the wind direction, and the first transect was performed as close to the fire as safety and logistical constraints allowed (6–48 km from the fire centroid). Background composition was also measured during turns between plume transects. This sampling strategy was repeated multiple times downwind of the plume. A pseudo-Lagrangian sampling strategy was attempted for smoke plumes using wind speed and wind direction to spatially and temporally position the aircraft to intercept the same portion of the smoke plume as it was transported downwind. These parameters were used to determine a physical age for each plume transect. During WE-CAN, the aircraft sampled downwind of targeted fresh smoke plumes with estimated physical ages as young as ~20 min and as old as ~10 h. Given the focus on near-source aging, the dataset is more robust for smoke plumes with physical ages spanning ~20 min to ~6 h (<185 km from the centroid of the active burn area). A pseudo-Lagrangian sampling strategy means that the maximum time a plume can be followed in time cannot exceed the flight time. In our case, this was often 4 h excluding transit to and from the airport. For cases closer to Boize, plumes could be repeatedly sampled for longer durations (>4 h). This sampling strategy is also intended to capture the chemical changes within a well-mixed smoke plume. The aircraft also intercepted air masses impacted by smoke from various unidentified sources in transit (shown in Figure 1), and we analyzed these data as a function of estimated chemical age and altitude. The WE-CAN campaign additionally targeted cloud-smoke mixtures.
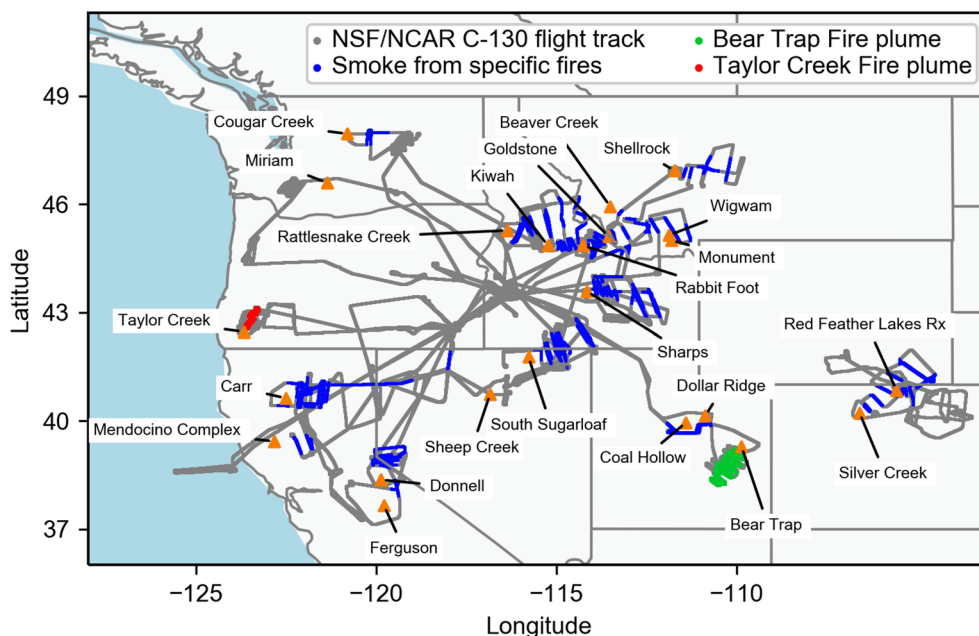
Figure 1. Flight tracks during WE-CAN (gray) with plume transects associated with specific, identifiable near-field fires (orange triangles) plotted in blue lines. Green and red lines indicate flight segments associated with smoke from the Bear Trap (August 9, 2018) and Taylor Creek (July 30, 2018) Fires, respectively.

Given that some of the reactive nitrogen instruments were not able to collect data during cloud-impacted time periods, we have excluded these from our analysis.

2.2. Instrument Descriptions

The WE-CAN payload included instrumentation to measure a large suite of gas-phase and aerosol-phase compounds. In this study, we use the following observations: NO and NO_2 measured using the NCAR 2-channel chemiluminescence instrument; PAN and PPN measured using the NCAR PAN-I-CIMS instrument; HONO, HNO_3, and Org $N_{(g)}$ (most likely multifunctional organic nitrates, peroxy nitrates, and/or peroxyacyl nitrates, see Section 2.2.3 for more details) measured using the University of Washington (UW) I-CIMS; NVOC (nitromethane, nitroethene, nitropropane, nitrofuran, nitrotoluene) measured using the University of Montana (UM) proton-transfer-reaction time-of-flight mass spectrometer (PTR-ToF-MS). There is no overlap between the gas-phase nitrogen-containing species measured by the UW I-CIMS (Org $N_{(g)}$) and by the UM PTR-ToF-MS (NVOC). Particulate nitrate (pNO_3) was measured using the CSU high-resolution time-of-flight aerosol mass spectrometer (HR-ToF-AMS). C_1–C_5 alkyl nitrates have been quantified by the NCAR Advanced Whole Air Sampler (AWAS) for the transects closest to the fires (Lindaas et al., 2020). They contribute a small fraction of the ΣNO_y and are not yet quantified for all smoke-impacted samples, so they are not included here. The small contribution of C_1–C_5 alkyl nitrates to ΣNO_y is consistent with prior observations. For example, H. B. Singh et al. (2010) report on measurements of total NO_y and the most abundant components of NO_y (i.e., NO_x, HNO_3, PANs, alkyl nitrates) during the ARCTAS campaign. C_1–C_5 alkyl nitrates comprise a small fraction (<10%) of the total measured NO_y. We use carbon monoxide (CO) as a conserved fire tracer that allows us to identify individual plume transects and correct for dilution. CO was measured by two different instruments: the NCAR QC-TILDAS and the NCAR Picarro. Volatile Organic Compounds (VOCs) were used to estimate the chemical age of the smoke and identify air masses influenced by urban emissions. The VOCs used in this analysis (HCN, CH_3CN, 2-methylfuran, acrolein, acrylonitrile, 2,2,4-trimethylpentane, tetrachloroethene, HFC-134a, and HCFC-22) were measured by the NCAR Trace Organic Gas Analyzer (TOGA). Photolysis frequencies were determined from the high-performance instrumented airborne platform for environmental research (HIAPER) Airborne Radiation—Actinic

Flux (HARP-Actinic Flux) instrument. The WE-CAN payload did not include a direct NO_y measurement. The following sections describe the instrumentation listed above.

2.2.1. NCAR NO_x/O_3

An NCAR 2-channel chemiluminescence instrument was used to measure NO and NO_2. Integrated with these instruments was a NCAR single-channel chemiluminescence instrument that measured O_3. These instruments share an inlet, pumping system, data acquisition system, and power supplies. NO is measured through its chemiluminescent reaction with a flow of reagent O_3, generated on board (Ridley & Grahek, 1990). Photons from the resulting excited NO_2 are counted with a dry-ice-cooled photomultiplier tube to provide the primary signal. NO_2 is measured in a separate sample flow as an increase in NO following photolysis of NO_2 by 400 nm light-emitting diodes (LEDs, model LZP-00UA00, bin code U5m with actual peak wavelengths of 390–395 nm and a spectral width of ~10 nm). Interferences from HONO on the NO_2 measurements are expected to be small given the factor of 40–150 larger NO_2 cross sections in the LED wavelength range. Periodic calibrations of the NO and NO_2 channels were performed during the flights. Two flows from a compressed gas calibration standard of NO in N_2 were used. One of the flows had O_3 added in order to convert NO to NO_2 for the calibration of the NO_2 conversion efficiency by the LEDs. Data are reported at 1 Hz, though the time response of the NO_x channels is somewhat slower than this (~2 s). At high mixing ratios (>1 ppbv), the uncertainties are 6% for NO and 12% for NO_2 and the upper bound on mixing ratio dependent precision is 100 pptv for NO and 140 pptv for NO_2.

2.2.2. NCAR PAN-CIMS

A thermal dissociation chemical ionization mass spectrometer (CIMS) was used to measure PAN and PPN (Slusher et al., 2004; Zheng et al., 2011). In the instrument inlet, PANs in ambient air are decomposed into NO_2 and the parent peroxy acyl (PA) radical at a temperature of 150°C. The latter reacts with iodine ions produced from trifluoroiodomethane (CF_3I) in a static ionizer cartridge in a flow tube controlled to a pressure of 20 Torr. A quadrupole mass spectrometer detects the produced acylate ions. A known amount of isotopically labeled ^{13}C-PAN is added to the aircraft inlet to perform continuous calibrations. Accuracy is 12% or 25 pptv (whichever is greater) for PAN and PPN, and precision is 20 pptv on average across the flight.

2.2.3. UW I-CIMS

The UW high-resolution chemical ionization time-of-flight mass spectrometer using iodide-adduct ionization (I-CIMS; Lee et al., 2014, 2018) was used to measure HNO_3, HONO, and a suite of other oxidized organic gases. Ambient air was sampled at 20 lpm through a straight ~50 cm length (0.75 in OD) PTFE Teflon tube. In order to minimize the influence of the tubing walls on the measurements and to characterize the remaining wall effects, the air was then subsampled at 2 slpm into a custom ion-molecule reaction (IMR) inlet (Palm et al., 2019). The mass spectrometer simultaneously measured hundreds of molecular formulas at 2 Hz time resolution and with a mass resolving power of ~5,000. Water vapor was continuously added to the IMR in order to maintain relatively constant water vapor concentrations and minimize the effects of water vapor dependence on the ionization process. The IMR background signal was measured for 6 s each 1 min by overflowing the IMR with clean N_2 gas. The tubing background signal was also measured for 15 s every 15 min. HNO_3 and HONO were each calibrated in the laboratory before and after WE-CAN deployment. Calibration factors and details specific to the WE-CAN deployment can be found in Peng et al. (2020), but in general are similar to those reported previously (Lee et al., 2014, 2018). Gas phase organic nitrogen-containing species measured by the I-CIMS were identified as any species containing nitrogen, two or more carbon atoms, and three or more oxygen atoms. The I-CIMS does not provide information on molecular structure or functional groups, but for this range of molecular formulas iodide-adduct ionization is most likely to be sensitive to multifunctional organic nitrates ($R-O-NO_2$), peroxy nitrates ($R-O-ONO_2$), and/or peroxyacyl nitrates ($R-COO-ONO2$) (Lee et al., 2016) (PAN and PPN like structures from the UW I-CIMS were excluded from this analysis to avoid overlap with the NCAR PAN-CIMS measurements). Multifunctional oxidized

amines cannot be ruled out but are expected to be minor. We also examined multifunctional nitroaromatic species, however, they comprise a small and consistent fraction (<1%) of the ΣNO_y and thus, are not included in the analysis. For these reasons and for simplicity, we refer to the sum of these I-CIMS measurements as gas phase organic nitrates (Org $N_{(g)}$). Since it is not feasible to individually calibrate for each organic nitrate species (or to determine their isomeric structures), we provide an estimate of the combined abundance of Org $N_{(g)}$ by assigning a calibration factor of five normalized counts per second (ncps) per ppt of analyte for all gas phase organic nitrates measured by the I-CIMS. This number was chosen as an estimate of the average sensitivity for this group of compounds, based on the range of sensitivity values of calibrated gases during WE-CAN. We estimate a factor of 2 uncertainty in the absolute concentration of the sum of Org $N_{(g)}$, although the trend within a plume over time is much less uncertain.

2.2.4. UM PTR-ToF-MS

VOC measurements were made with a proton-transfer-reaction time-of-flight mass spectrometer (PTR-ToF-MS 4000, Ionicon Analytik, Innsbruck, Austria). Briefly, atmospheric VOCs with a proton affinity higher than that of water (>165.2 kcal/mol) are ionized via proton-transfer reaction with H_3O^+ ions, and subsequently separated and detected by a time-of-flight mass spectrometer. PTR-ToF-MS measured ion m/z from 15 to 400 at 2 or 5 Hz frequency during WE-CAN. Ambient air was drawn to the instrument at 10–15 lpm via a ~3 m 1/4" (0.635 cm) O.D. PFA tube at ~55°C, and then subsampled by the instrument through a ~100 cm 1/16" (0.159 cm) O.D. PEEK tube at 60°C, resulting in less than 2 s for inlet residence time. Instrument background was checked in flight ~ hourly. Dynamic dilution of certified gas standard mixtures containing 25 VOCs including acetonitrile was used to perform calibrations 3 times each flight (Apel-Riemer Environmental Inc.). For ions not directly calibrated, sensitivities were estimated based on their molecular properties as described by Sekimoto et al. (2017). Measurement uncertainties for the 25 directly calibrated VOCs are ~15%; for the remaining compounds including many nitrogen (N) containing VOCs the uncertainty is estimated to be < 50%. Detection limits are species-specific and with the range of 50–250 pptv for VOCs with direct calibrations (Yuan et al., 2017). Our definition of NVOCs is any non-nitrate oxidized N-containing VOC that could be measured by the PTR (i.e., it does not include other NVOCs like acetonitrile, acrylonitrile, etc.). Specifically, the oxidized N-containing VOCs measured by the PTR are: nitromethane, nitroethene, nitropropane, nitrofuran, and nitrotoluene. These five compounds are what we refer to as NVOC.

2.2.5. CSU AMS

$p NO_3$ submicron non-refractory aerosol mass was measured by a high-resolution time-of-flight aerosol mass spectrometer (HR-TOF-AMS; Aerodyne, Inc.; DeCarlo et al., 2006) equipped with a pressure controlled inlet (Bahreini et al., 2008). Detailed description of the operation of this instrument and data processing during WE-CAN can be found in Garofalo et al. (2019). The time resolution for the measurements is 5 s. Accuracy (2σ) for inorganic species is estimated to be 35% (Bahreini et al., 2009). Given the nature of electron ionization, organic nitrates will fragment to NO_x^+ ions in the AMS, and thus may contribute to the reported $p NO_3$ (Farmer et al, 2010).

2.2.6. NCAR CO

CO was measured with a commercial Mini-TILDAS tunable diode laser infrared absorption spectrometer (Aerodyne Research; Lebegue et al., 2016). To optimize accuracy in the measurements, the spectrometer optical bench was continuously purged with synthetic zero grade air from which CO had been scrubbed to contain less than 1 ppbv. The WE-CAN data set has a precision of 100 ppt with a 2 s temporal resolution and an accuracy of ±0.6 ppbv for CO. A Picarro G-2401-m analyzer was used for the measurement of CO_2 and CH_4, which also provided an additional, but lower precision, measurement of CO. Stated 1-sigma precision for the Picarro is 30 ppb for CO. During the flights, regular calibrations were done by overflowing the inlet with a known mixture of the measured gases in ultra zero air.
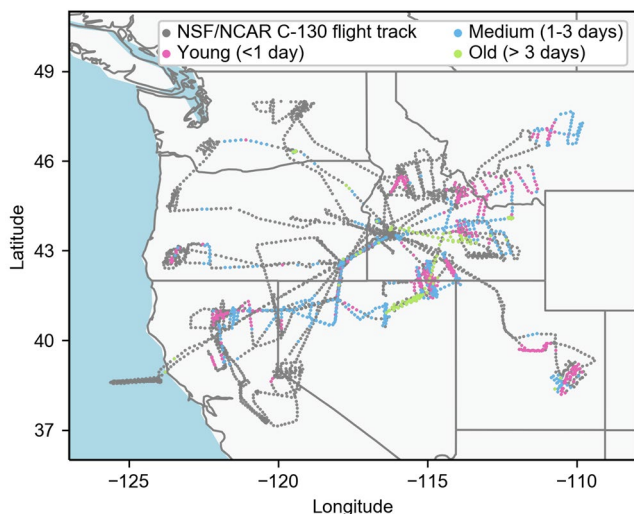
Figure 2. WE-CAN flight tracks colored by estimated plume chemical age on the TOGA instrument time resolution of an approximate 30-s sampling time with a 72-s gap between observations.

2.2.7. NCAR TOGA

TOGA, the Trace Organic Gas Analyzer, is a fast online gas chromatograph–mass spectrometer (GS-MS) instrument (Apel et al., 2003, 2015) that was used to measure a wide range of VOCs, some of which are used here. During WE-CAN, TOGA had a sample collection time of 28 s every 100 s for the first 11.5 research flights, and then transitioned to a 33-s sampling time every 105 s for the remainder of the research flights. The following TOGA measurements (uncertainties and detection limits in parentheses) were used to identify smoke-impacted observations, the chemical aging of those smoke-impacted observations, and as anthropogenic tracers: HCN (20%, 5 ppt), acetonitrile (CH_3CN; 40%, 10 ppt), 2-methylfuran (20%, 5 ppt), acrolein (30%, 0.5 ppt), acrylonitrile (50%, 1 ppt), 2,2,4-trimethylpentane (15%, 0.5 ppt), tetrachloroethene (15%, 0.5 ppt), chloroform (15%, 2 ppt), HFC-134a (50%, 1 ppt), and HCFC-22 (50%, 1 ppt).

2.2.8. HARP-Actinic Flux

Spectrally resolved actinic flux was measured with the HARP-Actinic Flux from 280–600 nm at a time resolution of 3 s. Hemispherical optical collectors connect via UV-enhanced fiber optic cables to charged-coupled device monochromators to provide simultaneous spectra. Photolysis frequencies for chemically relevant species were calculated from the actinic flux. The total uncertainties are specific to each molecule and are dominated by the corresponding molecular absorption cross section and quantum yield (e.g., 12% for jNO_2 and 15% for jHONO). More detailed information can be found in Shetter and Müller 1999.

2.3. Identification of Plumes

2.3.1. Identification of Fresh Smoke Plumes from Identified Fires and Physical Aging

The plume transects shown in Figure 2 are associated with known fires and are readily identified by sharp increases in CO, a common fire tracer with a summertime lifetime of at least 10 days (Holloway et al., 2000). The transects are defined as the portion of that plume transect where CO is above the 5th percentile for that crossing. We define a transect-specific background as the period when CO is below the 5th percentile. During this portion of the WE-CAN sampling, the science team tried to have the aircraft fully exit the plume before turning around to complete the next transect. We estimate a physical age for each plume transect by dividing the distance of the aircraft to the fire location by the average horizontal wind speed of that specific plume crossing. The fire location is defined as the centroid of the active burn area for that day. We note that there are uncertainties in the active burn area location and plume entrainment time (i.e., the time for the plume to be entrained into the mean flow). There is also variability in the wind speed (1) that each plume experienced as it rose to the altitude where it was intercepted by the aircraft, (2) along the plume trajectory, (3) across each sampling transect, and (4) before the C-130 arrived. Our approach likely yields the best practical estimate of total smoke age for each transect and even more accurate relative ages once a plume is entrained in the mean flow. In total, we identified and determined ages for 213 plume passes from 21 fires using this method.

In Section 3.1, we show results from 146 plume transects from 17 fires with physical ages ranging from 20 min to 6 h. This analysis includes 9 research flights (RF03, RF04, RF06, RF07, RF09, RF10, RF11, RF13, and RF15) which had complete data coverage for the individual ΣNO_y components (PTR-ToF-MS data was not available for RF15. However, we keep this flight in our analysis because the NVOC fraction is mostly constant along the entire dataset. See Section 3.1 for more details). We present the results as the partitioning of the sum of the normalized excess mixing ratios (NEMR) of the individual ΣNO_y components as a function of estimated physical age. The ΣNO_y NEMR is defined as the sum of the enhancements of the

individual ΣNO_y species divided by the CO enhancement. We use enhancement ratios in order to present a dilution-corrected view of the evolution of ΣNO_y across all the qualifying plumes transects sampled during WE-CAN. In Section 3.2, we present two case studies of specific smoke plumes.

2.3.2. Aged Smoke Identification and Chemical Aging

In addition to plumes from targeted fires, WE-CAN also sampled smoke-influenced air masses in transit, often from unidentified fires. Observations corresponding to CO > 85 ppbv, HCN > 275 pptv, and CH_3CN > 200 pptv are defined as smoke-influenced. We assign chemical ages to each of the smoke-influenced observations shown in Figure 1 according to the definitions given in O'Dell et al. (2020). The smoke-influenced observations were grouped by an approximate chemical age using co-sampled VOCs with different rate constants for loss via reaction with OH: 2-methylfuran, acrolein and acrylonitrile. These three VOCs, quantified by TOGA, were selected for assigning chemical age because they have high in-plume concentrations and their reaction rates with OH span a broad range. We have used the TOGA data for this analysis because TOGA has a lower detection limit for these species than the PTR-ToF-MS. The chemical age is defined according to a combination of the observed levels of 2-methylfuran, acrolein, or acrylonitrile. Smoke is categorized as "young" (<1 day of aging) when 2-methylfuran > 0.7 ppt (95th percentile of their respective background mixing ratios). Smoke is categorized as "medium" (1–3 days of aging) when 2-methylfuran is not elevated but acrolein is > 7.4 ppt (95th percentile of their respective background mixing ratios). Smoke is categorized as "old" (>3 days of aging) when neither 2-methylfuran nor acrolein are elevated, but acrylonitrile is > 2.9 ppt (95th percentile of their respective background mixing ratios). The "old" category also includes the few samples (15) when none of the VOC age tracers, (i.e., 2-methylfuran, acrolein or acrylonitrile) are elevated, but CO, HCN and CH_3CN are elevated (>85 ppbv, 275 pptv, and 200 pptv respectively). Samples where measurements of one of the fire tracers or the VOCs used for the aging were missing were excluded from this analysis. Samples with urban influence are removed when one of the following anthropogenic tracers (measured by TOGA) are elevated: 2,2,4-trimethylpentane (a fuel additive) (>20 pptv), tetrachloroethene (used in dry-cleaning and as a metal degreasing agent) (>2 pptv), HFC-134a (a refrigerant) (>125 pptv), or HCFC-22 (refrigerant) (>275 pptv) (ATSDR, EPA, Xing et al., 2014). Finally, these observations were also grouped by altitude reported in ASL (below 3 km, between 3 and 5 km, and above 5 km). Note that the data is more robust between 3 and 5 km, where most of the smoke was injected during the 2018 wildfire season.

Limitations of using these species for chemical aging include: (1) fast reaction of 2-methylfuran with NO_3 (Kind et al., 1996), which would reduce the quantitative age assigned to the "young" and "medium" categories, and (2) the chemical production of acrolein from alkenes, believed to be minimal compared to direct emissions of acrolein from fires (Apel et al., 2015). We acknowledge that the O'Dell et al. (2020) method of assigning approximate chemical age is sensitive to both variability in emissions from fires and dilution. Dilution effects could cause the mis-placement of younger, dilute smoke into an older category. For instance, some of the medium smoke samples are very dilute fresh smoke (i.e., young). O'Dell et al. (2020) explore the potential impacts of dilution on age assignment to show that the distribution of dilution-corrected tracers is similar to the non-dilution-corrected tracer distributions (see Figure S1.3 from O'Dell et al., 2020). Furthermore, O'Dell et al. (2020) found general agreement between this chemical age categorization and physical age estimates of fresh smoke plumes samples during WE-CAN. Thus, age uncertainties are unlikely to significantly impact our conclusions. We also note that all measurements are averaged over the TOGA sampling time, and TOGA collection times can encompass both smoke-impacted and background conditions or steep gradients in concentration. This can impact our assignment of chemical ages used here, and it is particularly relevant for narrow plumes. The width of the plumes (in terms of sampling time) ranged from 68 s to 10 min. For a more detailed discussion on this method of smoke-age assignment and its limitations, see O'Dell et al. (2020).
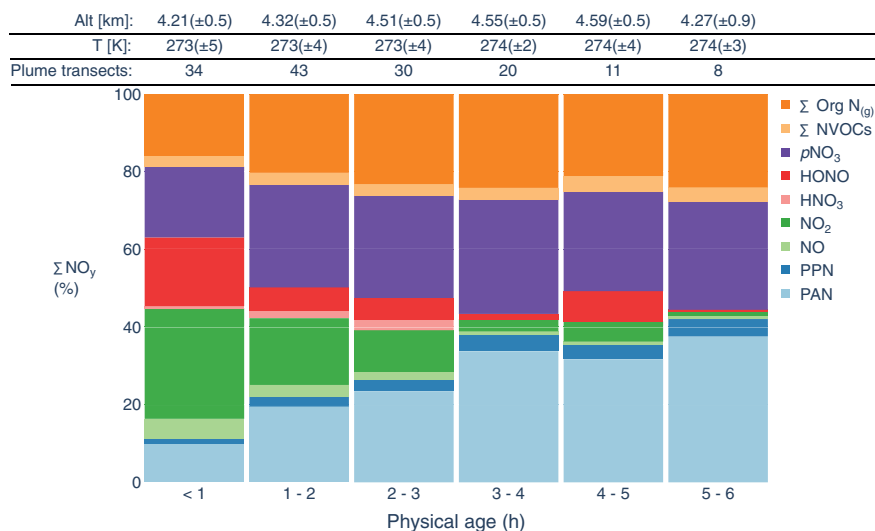
Alt [km]:	4.21(±0.5)	4.32(±0.5)	4.51(±0.5)	4.55(±0.5)	4.59(±0.5)	4.27(±0.9)
T [K]:	273(±5)	273(±4)	273(±4)	274(±2)	274(±4)	274(±3)
Plume transects:	34	43	30	20	11	8

Figure 3. Partitioning of ΣNO_y as a function of physical age in hours in the western U.S. wildfire smoke plumes sampled in a pseudo-Lagrangian fashion during WE-CAN. Each of the plumes included in this figure are associated with a specifically targeted fire (see Figure 2). The observations shown here correspond to sampling in the entire plume, which is defined as the portion of each plume transect where CO is above the 5th percentile of that transect. To calculate the enhancement of each species, a transect-specific background mixing ratio for each individual species is subtracted. Comparable figures for the most concentrated core of the plume and regions of the plume outside the concentrated cores are provided in Figures S1, S2, and S3.

3. Results and Discussion

3.1. Summary of ΣNO_y Partitioning in Near-Source Wildfire Plumes

Figure 3 shows a summary of quantified specific individual components of the ΣNO_y as a function of physical age in 146 smoke plume intercepts from 17 western U.S. wildfires sampled during WE-CAN. The plumes shown in Figure 3 were largely sampled above 3 km ASL with the exception of three plume transects from the Cougar Creek Fire (RF06) intercepted at lower altitudes (2.5–2.9 km ASL). The average temperature and altitude for each age category is shown on the top of the figure with the corresponding standard deviation in parentheses. Also note that the number of transects is largest closer to the fire; reflecting the scientific foci of WE-CAN as well as aircraft duty limitations. Figure 3 shows that NO_x is depleted quickly in large smoke plumes. On average after 3 h, NO_x contributes only 4%–7% of the ΣNO_y. Several studies have also observed the rapid decay of NO_x in wildfire plumes (Akagi et al., 2012; Alvarado et al., 2010; Hobbs et al., 2003; Jacob et al., 1992). This has also been observed in plumes emanating from agricultural fires; Liu et al. (2016) report that after ~30 min NO_x NEMRs drop between ~26% and ~56%. The average *e*-folding (decay) time and distance for NO_x for the smoke plumes sampled during WE-CAN and shown in Figure 3 is approximately 90 min of physical age, which corresponds to an average distance downwind of 40 km (Figures S4 and S5).

The median ratio of NO to NO_2 at the core of the plumes range from 0.11 to 0.24. This ratio varies as a function of time of day, with values >0.16 observed earlier in the day (i.e., the median ratio is 0.24 before 15:00 MDT) and values <0.2 observed later in the day as the photolysis rate of NO_2 decreases (i.e., the median ratio is 0.11 after 17:00 MDT) (Figure S6). Other chemical processes could also impact the NO to NO_2 ratio. Higher NO to NO_2 ratios have been observed in fresh smoke. Selimovic et al. (2018) report a NO to NO_2 ratio of ~2.3 in fresh smoke (5 s old) measured in the US Forest Service Fire Science Laboratory (FSL) as part of FIREX. Similarly, Akagi et al. (2012) report a NO to NO_2 ratio of 0.5 in smoke directly into the fire source (i.e., the mission could fly directly over the updraft and sample smoke a few minutes old). Peng et al. (2020) suggest that the daytime *e*-folding time for HONO is ~20 min in the fresh plumes sampled during WE-CAN, suggesting that HONO is depleted faster than NO_x in these plumes (see Figure 4 of this manuscript for specific examples). HONO emissions are the dominant OH source in the first ~1.5 h of observed fire plume evolution during which the most efficient radical ($HO_x = OH + HO_2$) production has happened. With
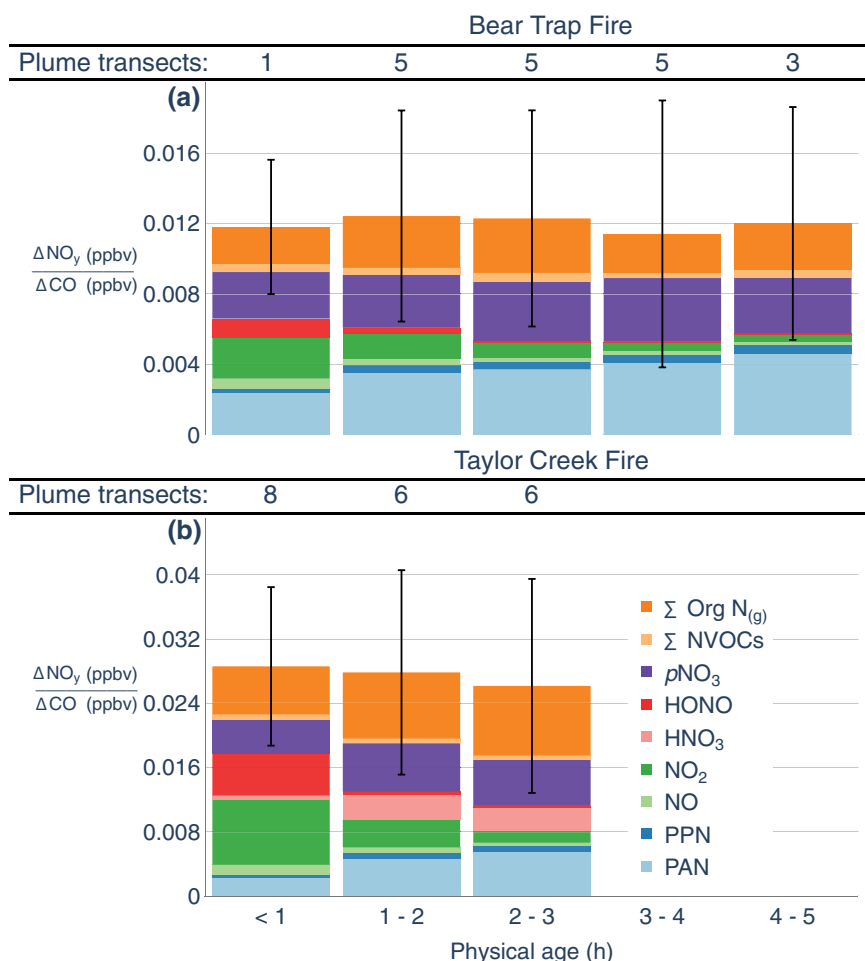
Figure 4. The sum of the individual NEMRs of ΣNO_y as a function of physical age (h) in the Bear Trap and Taylor Creek Fire smoke plumes sampled during WE-CAN. These smoke plumes were sampled in a pseudo-Lagrangian fashion twice. Here we present the average of the plume transects from both samples binned by their corresponding physical age. (See Section 2.3.1 for a discussion of uncertainty in the inputs to the calculation of physical age.) The plume transects are defined as in Figure 3, and a transect-specific background mixing ratio for each individual species was subtracted. The numbers above each bar signify the number of individual transects through the plume in each physical age bin. Error bars were calculated by adding the individual uncertainty for each NO_y species in quadrature.

the fast decay of HONO, the plumes become less photochemically active, and the overall absolute radical production drops substantially after 1.5 h. As a result, the relative contribution of HCHO and O_3 to radical production is more pronounced in these more aged plumes despite a much smaller absolute scale, as was also investigated by Peng et al. (2020). Photolysis rates across individual plume transects may vary. We have divided each plume transect in segments to represent the most concentrated and most diluted portions of the plume. Specifically, we divided each plume transect (as defined in Section 2.3.1) into core, edges, and wings. The core is defined as the portion of the plume where CO > 75th percentile. The edges of the plume are defined as the portions of the plume transect where 25th > CO > 75th percentile. Lastly, the wings of the plume are defined as the portions of the plume transect where 5th > CO > 25th percentile. The photolysis rates of NO_2 (jNO_2) and HONO ($jHONO$) decrease where the plume is more concentrated (i.e., core and edges) and later in the day as the sun is lower in the sky (Figure S7).

Compared to the measurements taken between 1 and 3 p.m. (LT), background jNO2 ($jHONO$) photolysis rates show a decrease of 15% (17%) in the "3–5 p.m." bin and 62% (64%) in the "5–7 p.m." bin. With respect to the appropriate background values for each plume transect, jNO2 ($jHONO$) reductions due to the smoke range from 20% to 40% (24%–42%) in the core of the plume, 3%–28% (4%–28%) within the edges of the

plume, and 1%–6% (1%–3%) within the wings of the plume. Larger percentage reductions in photolysis due to smoke were seen after 5p.m. The "5–7 p.m." bin shows overall jNO_2 reductions of 64%, 72%, and 77% in the wings, edges, and core, when compared to the afternoon "1–3 p.m." background values at higher sun. The partitioning of the ΣNO_y is similar between the core and edges of the plume. In the wings of the plume, where there is less light extinction and more background air entrainment, the partitioning of the ΣNO_y is substantially different from the core and edges of the plume. The main differences between the wings and core and edges of the plume are shown in Figures S1–S3. Closest to the fire (<1 h aging) there is no pNO_3 enhancement above background in the wings of the plume. After 1 h, the $NO:NO_2$ is higher in the wings than in the core of the plume, suggesting faster NO_2 photolysis (Figure S7). Finally, HNO_3 is considerably enhanced above background in the wings of the plume in physical ages between 1 and 3 h, suggesting less efficient condensation of HNO_3 to the particle phase (pNO_3) and entrainment of background air.

Averaged across all plume transects, approximately 37% of the ΣNO_y is in the form of PANs (PAN and PPN in this case) after 3 h. The rapid conversion of NO_x to PANs has been observed in several prior field campaigns targeting wildfire smoke. For example, Alvarado et al. (2010) reported on aircraft observations of boreal smoke plumes and showed that the average percent contributions of PAN to NO_y are 50% and 69% in fresh and aged smoke plumes, respectively. R J. Yokelson et al. (2009) reported on smoke plumes from a suite of tropical crop residue and deforestation fires. On average, they concluded that approximately 17% of NO_y was in the form of PAN following 1.2–1.4 h of aging. Akagi et al. (2012) reported aircraft observations of a prescribed California chaparral fire. They point out rapid initial growth of the PAN NEMR, based on observed increases of a factor of 10.7 (±5.3, standard deviation) in the first 4 h after emission. The rapid production of PAN has also been observed in agricultural fires (Liu et al., 2016). The PAN NEMR relative to NO_y increased from less than 5%–30% in ∼1 h; after ∼1.2 h, PAN accounted for 51%–74% of the loss of NO_x on a molar basis in a survey of 15 agricultural fires (Liu et al., 2016). Within the first 4 h following emission in the WE-CAN dataset, PAN accounts for 38% (±11%, standard deviation) of initial NO_x on a molar basis. Note that some of the prior studies (i.e., Akagi et al., 2012; Liu et al., 2016) sampled much smaller fires than those sampled during WE-CAN. Thus, these missions could fly directly through the updraft, and observe lower PAN/NO_x ratios in fresh smoke. The average PPN to PAN ratio in the core of the fresh plumes sampled during WE-CAN is 0.12 (±0.014, standard deviation).

HNO_3 mixing ratios within the center of these plumes, on average, are only slightly enhanced above background mixing ratios during the first 3 h of physical aging. After this point, the average enhancement of HNO_3 is zero or negative. This means that the background mixing ratio of this species is greater than the mixing ratio in the most concentrated part of the plume. As we show later, HNO_3 is often a substantial fraction of ΣNO_y in lower-altitude, warmer plumes. Trentmann et al. (2005) used a photochemical box-dilution model to show that the magnitude of the increase in pNO_3 observed during the Southern African Regional Science Initiative (SAFARI 2000) field experiment could be explained by the uptake of HNO_3 produced by gas-phase chemistry. As suggested by R. J. Yokelson et al. (2009), null or negative HNO_3 enhancements may be due to a rapid reaction of HNO_3 with NH_3 to form particulate ammonium nitrate. The process by which ammonium nitrate forms is mandated by the availability of NH_3 and HNO_3 and it is a strong function of temperature and humidity (Seinfeld & Pandis, 2006). In the concentrated cores of the WE-CAN plumes, the formation of ammonium nitrate may occur in the aqueous phase as well. Additionally, Tabazedah et al. (1998) proposed that biomass burning aerosols can remove HNO_3 in a similar way to sea salt aerosol, by HNO_3 replacing chloride (Cl^-) ions or water soluble organic ions such as formate, acetate, and oxalate present in biomass burning aerosols. Several studies have also noted that HNO_3 does not correlate with elevated CO in fresh or aged biomass burning smoke (e.g., Alvarado et al., 2010; Liu et al., 2016; R. J. Yokelson et al., 2009).

Figure 3 indicates that 18%–28% of the ΣNO_y is in the form of pNO_3 (purple bars in Figure 3), and that the evolution in the contribution of pNO_3 to ΣNO_y mirrors the evolution of PAN during the first 4 h. This result suggests rapid formation of pNO_3 in the first several hours of physical aging, similar to that observed by other studies (e.g., Akagi et al. [2012]; Hobbs et al. [2003]; Liu et al. [2016]; R. J. Yokelson et al. [2009]). The contribution of pNO_3 to ΣNO_y rapidly increases in the WE-CAN dataset from 18% to ∼26% in the first 2 h. The pNO_3 reported here by the AMS represents both organic and inorganic forms (Section 2.2.5). Work is ongoing to separate the inorganic fraction. One mechanism that contributes to rapid pNO_3 formation is the

reaction of HNO_3 and NH_3. The high abundances of NH_3 in the plume measured during WE-CAN suggest that the system was most of the time HNO_3 limited (with one exception that is discussed in Section 3.4) (Lindaas et al., 2020). Liu et al. (2016) also observed cases of rapid production of pNO_3 in agricultural fire smoke. They note that the pNO_3 in these smoke samples is mostly inorganic (>90%) as indicated by AMS measurements. Alvarado et al. (2010) reported contributions of 24% and 12% of pNO_3 to NO_y in fresh and old boreal smoke plumes, respectively. Similarly, Briggs et al. (2017) reported that pNO_3 contributed 20%–69% of the measured NO_y in 23 aged smoke plumes observed over the U.S. Pacific Northwest.

Despite relatively large measurement uncertainties, Figure 3 also shows that Org $N_{(g)}$ may comprise a large fraction (15%–26%) of ΣNO_y. Their collective evolution appears to mirror that of PANs and pNO_3, increasing their total contribution to ΣNO_y from 15% to ~23% within 3 h of physical aging. C_4 and C_5 organic nitrates contribute ~50% of the total abundance (in mixing ratio units); 80% of the total is from C_2–C_6 compounds (Figure S8). We expect that a dominant portion of the nitrophenolics are in the particle phase (Finewax et al., 2018; Matsumoto & Tanaka, 1996). The large contribution of Org $N_{(g)}$ to ΣNO_y in the WE-CAN dataset is not necessarily unexpected based on prior observations indicating that select individual organic nitrates (e.g., methyl peroxy nitrate) are present in smoke plumes intercepted under cold or high altitude conditions (Browne et al., 2011), and model simulations of smoke chemistry require more NO_x loss in the first several hours of plume evolution than can be explained by the formation of PAN or pNO_3 (Alvarado et al., 2015).

While also more uncertain than many of the other measurements summarized in Figure 3, the oxidized NVOCs quantified by the PTR-ToF-MS likely comprise a small and relatively consistent fraction of ΣNO_y as smoke plumes age. All comparable measurements of NVOCs in smoke are relatively recent and show that NVOCs comprise a small fraction of measured VOCs (e.g., Coggon et al., 2016; Gilman et al., 2015; Hatch et al., 2015; Koss et al., 2018; Liu et al., 2017, Roberts et al., 2020; Stockwell et al., 2015). For instance, Gilman et al. (2015) observed that NVOC (including reduced and oxidized forms) are a small fraction (<8%) of the total molar mass of VOC measured during laboratory burns. Methyl nitrite was the only oxidized NVOC reported as a dominant NVOC during these experiments.

We anticipate that the individual species that make up the ΣNO_y presented in this overview analysis comprise the majority of the total NO_y present in the wildfire smoke plumes sampled during WE-CAN. Our approach is different from many past studies in that we quantify ΣNO_y using individual contributors without a simultaneous total NO_y measurement, and the WE-CAN data represent much fresher smoke than some of the most relevant past studies. Other studies that have measured total NO_y (e.g., Briggs et al., 2017; H. B. Singh et al., 2012) have reported that ~80%–100% of the NO_y sampled in aged smoke plumes are in the form of peroxy nitrates (PNs), NO_x, pNO_3 and HNO_3. For instance, H. B. Singh et al. (2012) show that PNs, mostly in the form of PAN, comprise 60%–70% of the total NO_y during ARCTAS-A (spring) and ARCTAS-B (summer) in smoke plumes from boreal fires sampled after 3–8 days of aging. Some studies do report on select organic nitrate species. For example, in the smoke plumes sampled during ARCTAS-B and ARCTAS-CARB the total alkyl nitrates (ANs) comprise less than 10% of the measured NO_y. This percentage is lower than our estimates for Org $N_{(g)}$ which is between 15% and 26% for the plumes sampled during WE-CAN. Similarly, Briggs et al. (2017) report that NO_x, PAN, and pNO_3 comprise 77%–100% of the observed total NO_y in 4 wildfire smoke plumes observed over the U.S. Pacific Northwest after 1–2 days of aging. Thus, while our results are broadly consistent with this prior work, a comparison to past studies suggest that the uncertainties associated with total NO_y measurements, PAN, and HNO_3 observations in past studies, may have masked a potential substantial contribution to oxidized nitrogen from Org $N_{(g)}$ that is, visible in the WE-CAN data.

3.2. Case Studies of ΣNO_y Partitioning: Bear Trap (BT) and Taylor Creek (TC) Fires

Figure 4 presents the evolution of ΣNO_y in two individual smoke plumes emanating from the Bear Trap and Taylor Creek Fires; each of these plumes were repeatedly sampled in a pseudo-Lagrangian fashion. For these plumes, we present the absolute values for the NO_y NEMR rather than percentages to investigate ΣNO_y mass conservation with time. These plumes demonstrate variability in the total amount of oxidized nitrogen emitted and in the relative emissions of different N-containing species, a perspective that is somewhat masked in the average view presented in Figure 3. Proximity to the fire source, sampling altitude, meteorological conditions, modified combustion efficiency (MCE), and OH concentrations varied between

these plumes. From Figure 4, we can see that the dilution corrected abundance of ΣNO_y is conserved with time within the measurement uncertainties.

The Bear Trap Fire plume was sampled at approximately the same altitude for the first (~4.3 km) and second (~4.5 km) sampling sets. Temperature and relative humidity are approximately constant in the plume cores downwind ($\Delta T < 1$ K and $\Delta RH = 9\%$ across the samples included in the upper panel of Figure 4). The Taylor Creek Fire plume was much more narrow vertically, and the sampling altitude was less consistent as the mission attempted to intercept the plume at multiple altitudes. Thus, there are eight near-source transects with a mean estimated physical age of 35 min, ranging from 19 to 54 min. The sampling altitudes from the second pseudo-Lagrangian sampling effort of the Taylor Creek Fire plume encompass a wider range (3.3–4.5 km) because this set of intercepts includes a spiral through the plume. This sampling began further downwind; no intercepts represent <1 h of physical aging. As a result of these sampling choices, the temperature in Taylor Creek smoke plume intercepts (including the spiral) varies between 274 and 283 K (mean 281 K, ±2.2 standard deviation). Within the pseudo-Lagrangian sampling pattern (i.e., not the spiral), the temperature varies between 280 and 284 K (mean 282 K, ±1.2 standard deviation). The Taylor Creek Fire plume is also the driest smoke plume in the WE-CAN dataset ($3 < RH < 11\%$), thermodynamically favoring the presence of gas-phase HNO_3 over pNO_3 (Seinfeld & Pandis, 2006).

Figure 4 shows that, for both smoke plumes, the ratio of HONO to NO_x in the closest sampling passes is between 0.45 and 0.60 (ppbv ppbv^{-1}). Within 3 h, this ratio is on average 0.078 (±0.050 standard deviation) for both plumes, indicating that the photolysis of HONO occurs more rapidly than the overall conversion of NO_x to its oxidation products (Peng et al., 2020). Despite sampling these smoke plumes closer to the source than other fires targeted during WE-CAN, the samples still show substantial conversion of NO_x to its oxidation products in the closest sampling passes to the fire (blue, purple and orange bars in the leftmost columns of Figure 4). For instance, in the plume crossing closest to the Bear Trap Fire (physical age ~33 min), PANs, pNO_3, and Org $N_{(g)}$ comprise 20%, 22%, and 16% of ΣNO_y measured. These percentages are lower for the closest pass of the Taylor Creek Fire (physical age ~20 min), which are 4%, 11%, and 12% for PANs, pNO_3, and Org $N_{(g)}$, respectively. The PAN NEMR steadily increases in the Bear Trap Fire smoke plume through ~3–4 h of physical aging (~40% of the ΣNO_y). Similar to PAN, pNO_3 NEMR increases rapidly from 22% to 31% in 3–4 h of physical aging. The pattern of Org $N_{(g)}$ production in this case was different. The Org $N_{(g)}$ NEMR increases rapidly and stabilizes after 2 h (~23%), mainly driven by those with six or fewer carbon atoms. The detailed partitioning of Org $N_{(g)}$ across different carbon number groups are shown in Figure S9. For the Taylor Creek plume, we do not have samples out further than ~3 h of physical aging, but the PAN and Org $N_{(g)}$ NEMRs increase through ~3 h of physical aging and the pNO_3 NEMR stabilize after ~2 h. By the end of the sampling period, PAN and pNO_3 account for approximately the same percentage of ΣNO_y (~22%), and the Org $N_{(g)}$ make the largest contribution to ΣNO_y (~33%).

Liu et al. (2016) observed similar production rates for PAN and pNO_3 in the first hour of smoke evolution from five individual agricultural fires. Even though these agricultural fires were relatively small, and the smoke was less dense than the plume cores included in Figure 4, Liu et al. (2016) also found that by the end of the sampling periods (~30–50 min) PAN and pNO_3 accounted for approximately the same fraction of the total NO_y. However, they also encountered two fires where a larger fraction of NO_x converted to pNO_3 instead of forming PAN by the end of the sampling period (~1 h). The evolution of $\Delta pNO_3/\Delta PAN$ as a function of physical age for each of the Bear Trap Fire and Taylor Creek Fire smoke plumes can be described with an exponential decay function (Figure S10). For the Taylor Creek Fire plume, this ratio is ~3 at 30 min and drops to ~0.7 by ~1.5 h of physical aging. For the Bear Trap Fire, this ratio is slightly >1 at 30 min and drops to ~0.6 after 4 h of sampling, signifying faster PAN production in aged smoke, but faster pNO_3 production at the outset. Consistent without results, Liu et al. (2016) report the same ratio as slightly >1 after 1 h of physical aging and Akagi et al. (2012) and Alvarado et al. (2010) report $\Delta pNO_3/\Delta PAN$ of ~0.75 and ~0.5 in more aged plumes (4–10 h) from chaparral and boreal fires, respectively.

Of the two example plumes shown here, the Taylor Creek Fire produced larger emissions of ΣNO_y relative to CO (0.030 ppbv ppbv^{-1}), more than twice that of the Bear Trap Fire (0.012 ppbv ppbv^{-1}). We calculated the MCE for each fire following Lindaas et al. (2020). The Bear Trap Fire had an average MCE of 0.88 (±0.017, standard deviation) indicating that the plume contained emissions produced from both smoldering and flaming conditions. This is reflected in the higher relative abundance of reduced forms of nitrogen

(Lindaas et al., 2020). The Taylor Creek Fire had an average MCE of 0.94 ($\pm$0.003, standard deviation) indicating that the plume represents more flaming conditions and efficient combustion. This plume has one of the highest MCE of all the plumes sampled during WE-CAN, suggesting emission of more oxidized forms of reactive nitrogen (i.e., NO_x and HONO) and less of reduced forms of reactive nitrogen (i.e., NH_3). Despite the difference in MCE between fires, the relative contribution of pNO_3 to ΣNO_y is not substantially different between these plumes, as was discussed above. However, distinguishable HNO_3 enhancements (up to 2.1 ppbv) above background were present in the Taylor Creek plume for the duration of the sampling period; HNO_3 accounts for $\sim$10% of ΣNO_y, even after 3 h of physical aging. Tabazadeh et al. (1998) and Trentmann et al. (2005) suggest that an important sink for HNO_3 in plumes is scavenging by particles. Even at an RH of 15% and temperature of 220 K, dust particles contain sufficient liquid water for the displacement of carbonate by NO_3^- ions to occur (Tabazadeh et al., 1998). Cl^- replacement by the NO_3^- ion can also occur in smoke plumes as smoke particles have a significant mass fraction of water present (Tabazadeh et al., 1998). A reduction in Cl^- mass percentage in smoke particles was observed by R. J. Yokelson et al. (2009), Akagi et al. (2012), and Kleinman et al. (2020). One potential reason that the Taylor Creek Fire plume contained excess HNO_3 may be because of the simultaneously dry conditions; the scavenging of HNO_3 by particles may not have been as efficient as in other smoke plumes. Additionally, the production of NH_4NO_3 in the smoke plume of the Taylor Creek Fire might have been impacted by other factors. The flaming condition (MCE = 0.94) of this fire resulted in higher emissions of oxidized over reduced forms of reactive nitrogen limiting the availability of NH_3 to form NH_4NO_3 as the plume ages (Lindaas et al., under review). The abundance of organic and inorganic particulate sulfate (pSO_4) is 1–2 orders of magnitude higher in the Taylor Creek Fire than in the Bear Trap Fire plume; thus, sulfate had the potential to impact the free NH_3 initially available in the system to form NH_4NO_3. In this plume, NH_3 enhancements become smaller than HNO_3 enhancements after 2 h of physical aging, whereas in the Bear Trap Fire plume, the system remains HNO_3 limited for the duration of the sampling. The Taylor Creek Fire plume is a special case among the plumes sampled during WE-CAN given the warmer and drier conditions of the plume, relatively low NH_3 emissions, and high pSO_4 abundance, all resulting in positive HNO_3 enhancements.

We estimate an OH concentration for these plumes via two methods. The first method is described by Hobbs et al. (2003). To do this, we assume that the loss rate of the NEMR of toluene and benzene is dominated by reaction with OH (Equation S1 and Figures S11 and S12). To apply the Hobbs et al. (2003) method to the short timescales of interest, we need a set of VOCs with different, but also relatively short (i.e., minutes to hours) lifetimes against oxidation by OH. As a shortcut we also prescribed OH, and then iterated on that prescribed value, to match the observed decay of butene and methyl furans, significantly shorter-lived species with large primary emissions. We know that the actual OH concentration changes rapidly in smoke plumes (Peng et al., 2020), but the average OH concentration for the Bear Trap Fire and Taylor Creek Fire smoke plumes calculated via the first (second) method are 4×10^6 (2×10^6) molecules cm^{-3} and 1×10^7 (5.5×10^6) molecules cm^{-3}, respectively. The production of HNO_3 by the reaction of NO_2 with OH is an important sink for NO_x. At the average temperatures and pressures of the Bear Trap Fire and Taylor Creek Fire smoke plumes (275 K and 573 hPa, and 281 K and 644 hPa, respectively) and the two different OH estimates (estimates from second method in parenthesis), the pseudo first order rate coefficients for this association reaction are 3.74×10^{-5} (1.88×10^{-5}) s^{-1} and 9.54×10^{-5} (5.25×10^{-5}) s^{-1} which result in average NO_2 lifetimes against OH oxidation of $\sim$7.4–14.8 and $\sim$2.9–5.3 h for the Bear Trap Fire and Taylor Creek Fire smoke plumes, respectively. The value reported by Akagi et al. (2012) for the Williams Fire plume ($\sim$5.1 h) is between our two estimates.

In the time these two plumes were observed ($\sim$4.4 and $\sim$2.6 h for Bear Trap Fire and Taylor Creek Fire smoke plumes, respectively), we estimate, assuming no other loss paths for NO_x, that 55%–75% and 40%–60% of the initial NO_x would be converted to HNO_3 (or pNO_3). In the Taylor Creek Fire plume, after 2.6 h of sampling, the total observed increase in $HNO_3 + pNO_3$ accounts for $\sim$41% of the initial NO_x (matching our estimate). On the other hand, in the Bear Trap Fire plume, after 4.4 h of sampling, the observed increase in pNO_3 (no HNO_3 enhancement was observed in this plume) accounts for only 20% of the initial NO_x. This suggests that in the Bear Trap plume either a competitive pathway for NO_x loss dominated and/or that our assumptions of OH are not realistic. Finally, we examined the loss of NO_x and HONO and compared it to the production of PANs, pNO_3, and Org $N_{(g)}$ for the duration of the sampling of each of these fires (Table 1). In the case of the Bear Trap Fire, the production of PANs, pNO_3, and Org $N_{(g)}$ (0.0029 ppbv $ppbv^{-1}$) accounts

Table 1
Summary Sampling and Chemical Differences Between the Bear Trap Fire and Taylor Creek Fire

Observed or estimated parameter	Bear Trap Fire	Taylor Creek Fire
(OH)	4×10^6, 2×10^6 (molec cm^{-3})	1×10^7, 5.5×10^6 (molec cm^{-3})
NO_2 $t_{1/2}$	7.4, 14.8 (h)	2.9, 5.3 (h)
Maximum physical age (h)	4.4 (h)	2.6 (h)
Loss NO_2 + OH (calculated)	55%–75%	40%–60%
Prod NO_2 + OH (observed)	20%	41%
Loss $\dfrac{\Delta NO + \Delta NO_2 + \Delta HONO}{\Delta CO}$	0.0026 (ppbv ppbv^{-1})	0.0067 (ppbv ppbv^{-1})
Prod $\dfrac{\Delta PANs + \Delta pNO_3 + \Delta OrgN_{(g)}}{\Delta CO}$	0.0029 (ppbv ppbv^{-1})	0.0052 (ppbv ppbv^{-1})

for all the loss in NO_x and HONO (0.0026 ppbv ppbv^{-1}). However, for the Taylor Creek Fire, the production of PANs, pNO$_3$, and Org N$_{(g)}$ (0.0052 ppbv ppbv^{-1}) accounts for only ∼80% of the loss in NO_x and HONO (0.0067 ppbv ppbv^{-1}), suggesting the presence of other NO_x oxidation products in this smoke plume.

3.3. ΣNO$_y$ Partitioning Across the Entire WE-CAN Smoke Dataset

There is considerable variability in the composition and abundances of ΣNO$_y$ across the entire WE-CAN dataset which includes measurements of young, medium and old smoke observations sampled at different altitudes. The smoke flight segments presented in Figure 5 include samples from both fresh plumes attributed to known fires and diluted smoke intercepted outside of pseudo-Lagrangian sampling efforts. We use the median value of the out of smoke samples as an assumed background to calculate the ΣNO$_y$ enhancement ratios for each altitude bin.

The amount of PANs present in the smoke samples increases with increasing altitude (note different y-axes in Figure 5), which is consistent with the temperature-dependent lifetime of these compounds (Singh, 1987). The contribution of PANs to ΣNO$_y$ also increases with age within the individual altitude bins. Briggs et al. (2017) observed 25%–57% of NO$_y$ as PAN in aged smoke plumes from regional fires observed in Oregon in summers 2012 and 2013. These numbers are within the range observed in the WE-CAN data set where PAN accounts for 24%–36% of ΣNO$_y$ in the medium and old smoke samples.

Org N$_{(g)}$ comprise a large fraction (∼32–40%) of the smoke samples below 3 km and their contribution to ΣNO$_y$ decreases with altitude. Across the smoke dataset, the contribution of HNO$_3$ to ΣNO$_y$ is small (<4%) or zero at all altitudes and chemical age bins. The measured contribution of pNO$_3$ to ΣNO$_y$ varies with altitude and age bin. Below 3 km, pNO$_3$ contribution to ΣNO$_y$ decreases with age, suggesting that as smoke dilutes it favors the volatilization of HNO$_3$ to the gas-phase. Conversely, above 3 km, pNO$_3$ contribution to ΣNO$_y$ generally increases with age (and the enhancement mixing ratios remain mostly constant between the medium and old age bins), suggesting favorable conditions (e.g., low temperature) for pNO3 stability above 3 km. Consistent with this finding, Wu et al. (2020) also found an increase in particulate inorganic nitrate mass fraction with altitude in the free troposphere. Finally, and consistent with Figure 3, HONO is only enhanced above background levels in the youngest chemical age bins in smoke samples above 3 km. When a background is subtracted from smoke-impacted air masses (as in Figure 5), it can mask some interesting relationships between individual NO$_y$ species (e.g., HNO$_3$ and pNO$_3$). Therefore we have included a version of Figure 5 in the SI (Figure S13) with its corresponding interpretation that shows the ΣNO$_y$ partitioning without a background subtraction.
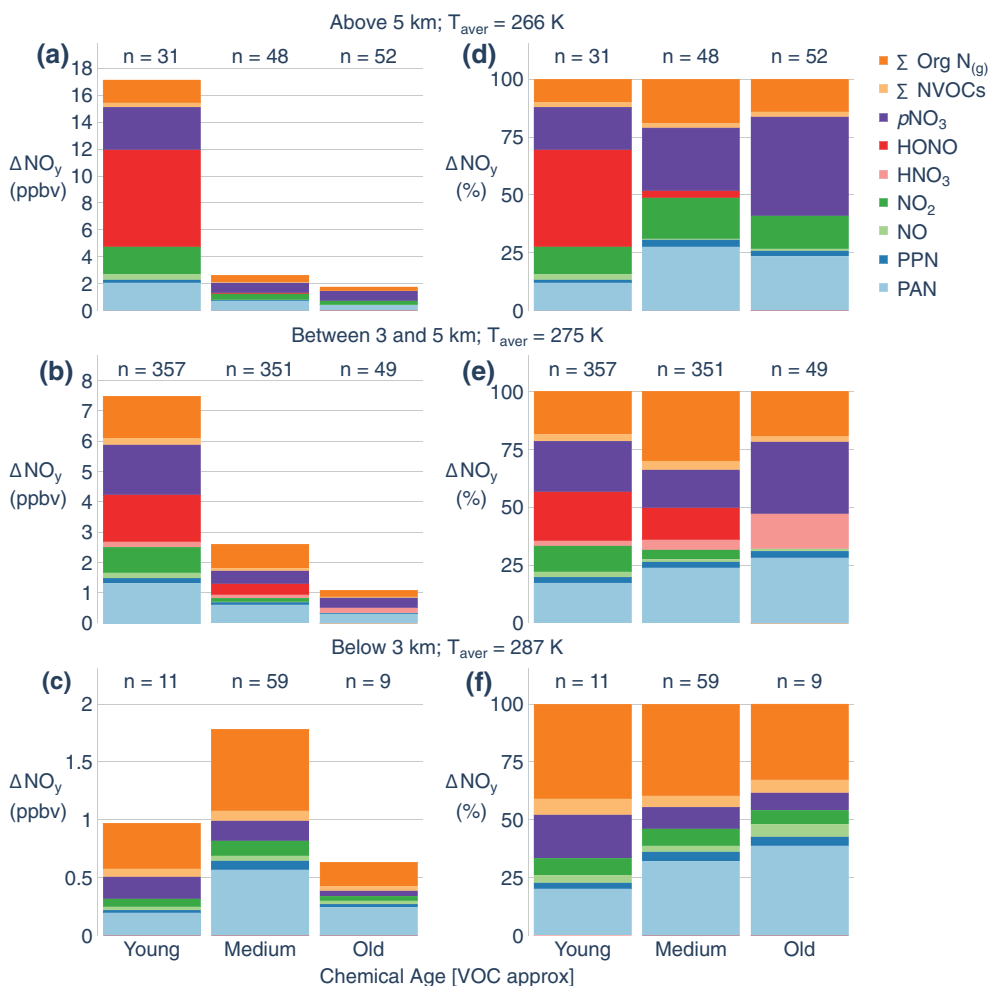
Figure 5. ΣNO_y of smoke samples within the full WE-CAN dataset. TOGA time-base samples are binned by an approximate chemical age: young (<1 day of aging), medium (1–3 days of aging) and old (>3 days of aging) as described in Section 2.3.2. Samples are also binned by sampling altitude, and the average temperature of the samples in each category is provided. The columns in the left panels represent the enhancement of ΣNO_y (note different y-axis in Figure 5) and are shown as percentages in the right panels. The number above each bar represents the number of individual TOGA time segments in each category, not individual plume transects. The majority of samples were collected between 3 and 5 km ASL. A smaller number of samples were collected below 3 km, due to safety and logistical constraints of operating the aircraft in low visibility conditions and high terrain elevation where most of the fires were located; and above 5 km given that most of the plumes were injected between 3 and 5. Therefore, the data presented in Figures 5 and S13 is more robust between 3 and 5 km. Samples that are substantially influenced by fresh anthropogenic emissions (see Section 2.3.2) are not included in this analysis. The scheme described in Section 2.3.2 would not identify agriculturally influenced samples. Note that the majority of the young and medium smoke samples (i.e., left-most bars) coincide with the plumes presented in Figure 3. The medium category includes a small number of smoke samples from very dilute fresh smoke (i.e., wing of the plume).

3.4. ΣNO_y Partitioning in the Smoke-Impacted California Central Valley

The NSF/NCAR C-130 performed a dedicated flight over the California Central Valley during a period when smoke from multiple fire complexes impacted the region. Here we focus on the subset of data collected in this region that has been assigned ages as previously discussed in Sections 2.3.2 and 3.3. The aircraft performed a combination of low-level legs and two sets of missed approaches at three different airports in the region: Chico Municipal Airport (KCIC; 39.7991 N, 121.8548 W), Mather Airport (KMHR; 38.5637 N; 121.2972 W), and Merced County Castle Airport (KMER; 37.3735 N; 120.5731 W). There were many layers of smoke in the Central Valley, and the aircraft did not specifically target a particular smoke plume during this flight, but sampled smoke from the Carr Fire, the Mendocino Complex, and several fires located near

Yosemite National Park. Most of the smoke was intercepted below 3 km (mean temperature = 300 K). The WE-CAN data shows that HNO_3 is the dominant NO_y species in the smoke-impacted samples collected over the Central Valley, accounting for ~60% of the total NO_y. This is consistent with the overall picture shown in Figure S13 and the unfavorable warm conditions for PAN (Singh, 1987) and pNO_3 (Seinfeld & Pandis, 2006). Gas-phase organic nitrates, PAN, and NO_2 are the next most abundant NO_y species accounting for 16%, 10%, and 9%, respectively. Finally, the contributions from pNO_3, NO, PPN, and oxidized NVOCs were minor, individually contributing ~1%–3% of the total NO_y measured over the Central Valley.

The NASA DC-8 research aircraft outfitted with a similar suite of instrumentation sampled this same geographical region during the ARCTAS-CARB field campaign in June 2008 (Jacob et al., 2010), another period with large wildfires in northern California. Using similar data collected below 3 km and between 12:00 and 16:00 PDT, we are able to compare NO_x, PAN and $NO:NO_2$ ratios as a function of CH_3CN with those measured by H. B. Singh et al. (2012) in 2008. We note that the WE-CAN data was collected later in the day, between 13:30 and 17:00 PDT. Figure 4 of H. B. Singh et al. (2012) report the mean relative NO_x enhancement mixing ratios of 2 ppb in 12 plumes with considerable fire influence and 5 ppb in 7 plumes with high anthropogenic influence but minimal fire influence. Higher NO_x mixing ratios are also observed in the Central Valley flight during WE-CAN when smoke is mixed with anthropogenic emissions, denoted in Figure 6 as samples with elevated chloroform (3-methyl-pentane, tetrachloroethylene, HFC-134a, HCFC-141b, and HCFC-22 were also elevated in these samples). In these instances, NO_x mixing ratios in smoke-urban mixtures increased by ~1 ppbv on average (and up to ~3.5 ppbv). H. B. Singh et al. (2012) observed decreasing $NO:NO_2$ ratios with increasing smoke contribution. The $NO:NO_2$ ratios observed over the California Central Valley during WE-CAN are not consistent with the pattern in H. B. Singh et al. (2012). This ratio is also not systematically perturbed in more anthropogenically influenced air masses (i.e., points with elevated chloroform).

We also compared PAN mixing ratios between the WE-CAN data set and the data reported by H. B. Singh et al. (2012). Both show a strong relationship between PAN and CH_3CN. Samples with more PAN relative to CH_3CN in the WE-CAN data set appear to be the result of injections of anthropogenic NO_x emissions. For the same CH_3CN mixing ratio, there can be twice as much PAN when smoke is mixed with urban emissions. pNO_3 abundances in the California Central Valley also increase with increasing fire influence (i.e., higher CH_3CN mixing ratios). There are pNO_3 outliers when anthropogenic NO_x emissions mix with smoke. However, the relative change is much smaller than what was observed for NO_x and PAN.

4. Conclusions

The WE-CAN field campaign utilized the NSF/NCAR C-130 to systematically build a dataset of afternoon smoke observations. The WE-CAN observations include more than 200 plume transects that can be connected to >20 different unique identified specific fires and an additional set of smoke samples from a wider set of fires. The full dataset affords the opportunity to examine the evolution of oxidized reactive nitrogen in western U.S. smoke plumes over timescales of hours to days.

1. We find that daytime emissions of NO_x and HONO from wildfires are rapidly transformed to more oxidized forms of NO_y (pNO_3, PANs, and Org $N_{(g)}$) within the first few hours of physical aging in the plumes sampled during WE-CAN. After ~2 h the fraction of ΣNO_y in the form of pNO_3 approximately doubled, and after ~4 h the dilution corrected abundances of PANs plateau. After ~4 h NO_x and HONO together account for a small fraction (<10%) of ΣNO_y, and pNO_3, PANs, and gas-phase organic nitrates become the dominant contributors to ΣNO_y, contributing on average ~26 %, ~37%, and ~23%, respectively. Little to no enhancement of HNO_3 is typically observed in the near-source (<6 h of aging) wildfire smoke plumes (suggesting either rapid association with NH_3 (when favorable) to form NH_4NO_3 or effective scavenging by other heterogeneous aerosol chemistry).

2. Significant differences are observed between the Bear Trap Fire and Taylor Creek Fire smoke plumes. These two fires were successfully and repeatedly sampled in a pseudo-Lagrangian fashion and both show ΣNO_y mass conservation (within the uncertainties of the measurements) for the duration of the sampling. Variability in sampling conditions include differences in proximities to the fire source, plume heights, atmospheric conditions (temperature and relative humidity), MCE, and estimated OH
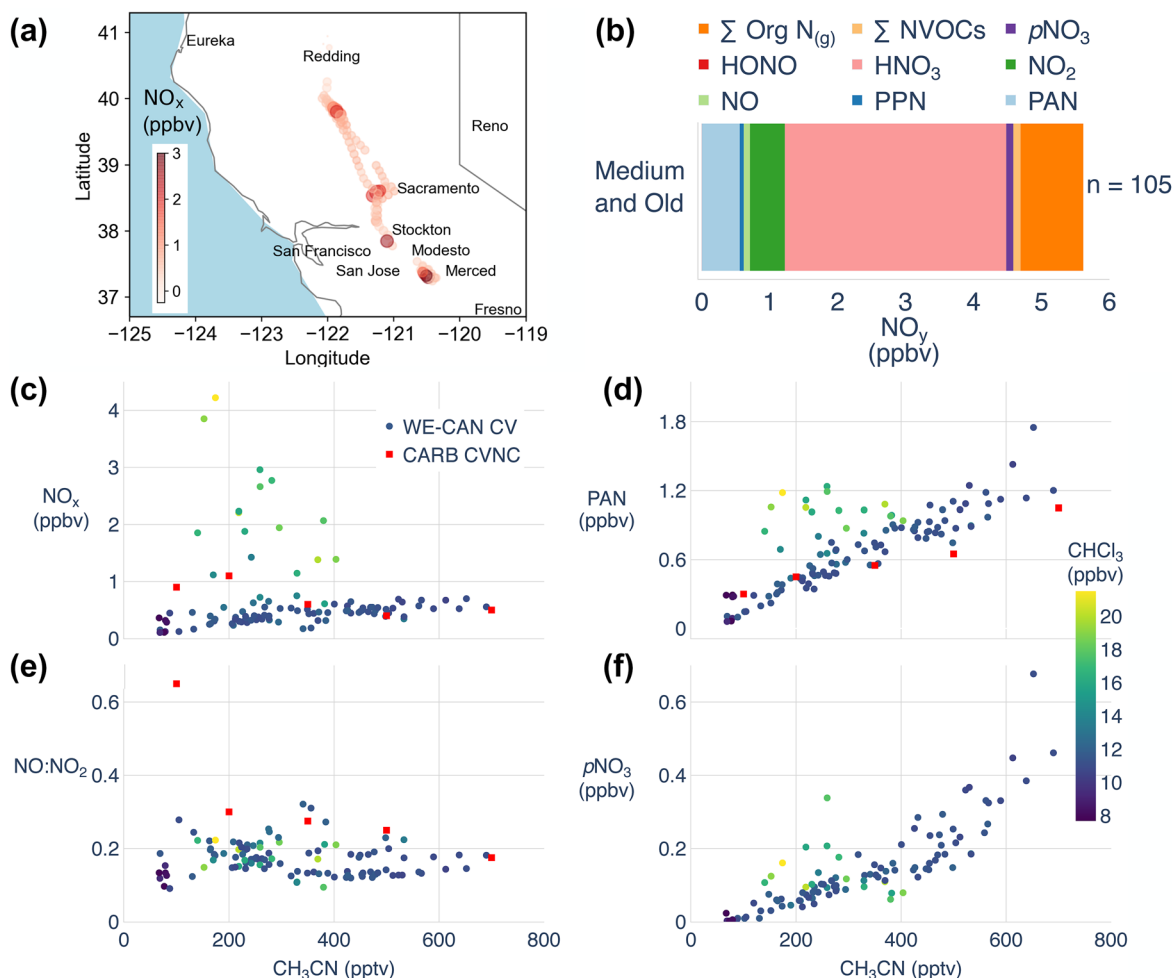
Figure 6. (a) NSF/NCAR C-130 flight track through the California Central Valley (CV) on August 8, 2018 colored by NO_x mixing ratio (ppbv). (b) The inset bar shows the NO_y partitioning for all the medium and old smoke-impacted samples shown in (a). There were no samples classified as young based on the criteria in Section 2.3.2. Data were collected between 13:30 and 17:00 PDT. The average ΣNO_y mixing ratio in the smoke impacted Central Valley was ~5.5 ppbv, with little difference between the medium and old categories. Therefore, we show their partitioning together as one inset bar. (c)–(e) Scatterplots of NO_x, PAN, $NO:NO_2$, and pNO_3 vs. CH_3CN for the flight segment through the region are shown in (a). These panels are colored by chloroform ($CHCl_3$). Shown in red squares are NO_x (c), PAN (d), and $NO:NO_2$ (e) observed during ARCTAS-CARB (H. B. Singh et al., 2012).

concentration. The higher MCE Taylor Creek Fire smoke plume samples contain almost twice as much ΣNO_y relative to CO than the Bear Trap Fire smoke plume samples. The Taylor Creek Fire smoke plume, characterized by exceptionally low RH (3%–11%), warmer conditions, and low abundances of NH_3 (Lindaas et al., 2020) is the only young plume sampled in a pseudo-Lagrangian fashion during WE-CAN that contains HNO_3 enhancements above background conditions.

3. The partitioning of ΣNOy in all the smoke samples intercepted during WE-CAN varies with altitude. These samples include smoke samples outside the pseudo-Lagrangian sampling efforts. Above 3 km, HONO is only elevated above the detection limit in young and medium smoke samples. The abundance of PANs increases with altitude in the smoke samples. Below 3 km, Org $N_{(g)}$ are a large fraction of ΣNO_y. Finally, the behavior of pNO_3 varies with altitude. Below 3 km, the relative abundance of pNO_3 is much lower than smoke samples intercepted at higher altitudes and its contribution to ΣNO_y decreases with chemical age. Above 3 km, the relative contribution of pNO_3 to ΣNO_y increases as the samples chemically age.

4. WE-CAN also sampled smoke from multiple fires mixed with anthropogenic emissions over the California Central Valley. In these mixed smoke plumes, predominantly sampled below 3 km, additional injections of anthropogenic NO_x (and secondary PAN) can be distinguished by examining relationships

between these species and CH_3CN. For this specific day, injections of anthropogenic emissions provided additional NO_x, increasing the abundance by up to a factor of 4. Anthropogenic NO_x appears to contribute to additional PAN formation. The NO to NO_2 ratio in the smoke-filled Central Valley does not appear to be affected by injections of anthropogenic emissions during the afternoon.

Our analysis provides a comprehensive look at the partitioning of ΣNO_y in wildfire smoke plumes and smoke-impacted samples over the western U.S. during summer 2018, providing organized data for the modeling community to further investigate the processes controlling the evolution of NO_y in smoke.

Data Availability Statement

Data are available in the WE-CAN data archive (https://data.eol.ucar.edu/master_lists/generated/we-can/). The authors declare no conflicts of interest.

References

Akagi, S. K., Craven, J. S., Taylor, J. W., McMeeking, G. R., Yokelson, R. J., Burling, I. R., et al. (2012). Evolution of trace gases and particles emitted by a chaparral fire in California. *Atmospheric Chemistry and Physics*, *12*(3), 1397–1421. https://doi.org/10.5194/acp-12-1397-2012

Akagi, S. K., Yokelson, R. J., Burling, I. R., Meinardi, S., Simpson, I., Blake, D. R., et al. (2013). Measurements of reactive trace gases and variable O3 formation rates in some South Carolina biomass burning plumes. *Atmospheric Chemistry and Physics*, *13*(3), 1141–1165. https://doi.org/10.5194/acp-13-1141-2013

Akagi, S. K., Yokelson, R. J., Wiedinmyer, C., Alvarado, M. J., Reid, J. S., Karl, T., et al. (2011). Emission factors for open and domestic biomass burning for use in atmospheric models. *Atmospheric Chemistry and Physics*, *11*(9), 4039–4072. https://doi.org/10.5194/acp-11-4039-2011

Alvarado, M. J., Logan, J. A., Mao, J., Apel, E., Riemer, D., Blake, D., et al. (2010). Nitrogen oxides and PAN in plumes from boreal fires during ARCTAS-B and their impact on ozone: An integrated analysis of aircraft and satellite observations. *Atmospheric Chemistry and Physics*, *10*(20), 9739–9760. https://doi.org/10.5194/acp-10-9739-2010

Alvarado, M. J., Lonsdale, C. R., Yokelson, R. J., Akagi, S. K., Coe, H., Craven, J. S., et al. (2015). Investigating the links between ozone and organic aerosol chemistry in a biomass burning plume from a prescribed fire in California chaparral. *Atmospheric Chemistry and Physics*, *15*(12), 6667–6688. https://doi.org/10.5194/acp-15-6667-2015

Andreae, M. O. (2019). Emission of trace gases and aerosols from biomass burning—An updated assessment. *Atmospheric Chemistry and Physics*, *19*(13), 8523–8546. https://doi.org/10.5194/acp-19-8523-2019

Andreae, M. O., & Merlet, P. (2001). Emission of trace gases and aerosols from biomass burning. *Global Biogeochemical Cycles*, *15*(4), 955–966. https://doi.org/10.1029/2000GB001382

Apel, E. C., Hills, A. J., Lueb, R., Zindel, S., Eisele, S., & Riemer, D. D. (2003). A fast-GC/MS system to measure C_2 to C_4 carbonyls and methanol aboard aircraft. *Journal of Geophysical Research*, *108*(D20), 8794. https://doi.org/10.1029/2002JD003199

Apel, E. C., Hornbrook, R. S., Hills, A. J., Blake, N. J., Barth, M. C., Weinheimer, A., et al. (2015). Upper tropospheric ozone production from lightning NO_x-impacted convection: Smoke ingestion case study from the DC3 campaign. *Journal of Geophysical Research: Atmospheres*, *120*(6), 2505–2523. https://doi.org/10.1002/2014JD022121

Bahreini, R., Dunlea, E. J., Matthew, B. M., Simons, C., Docherty, K. S., DeCarlo, P. F., et al. (2008). Design and operation of a pressure-controlled inlet for airborne sampling with an aerodynamic aerosol lens. *Aerosol Science and Technology*, *42*(6), 465–471. https://doi.org/10.1080/02786820802178514

Bahreini, R., Ervens, B., Middlebrook, A. M., Warneke, C., de Gouw, J. A., DeCarlo, P. F., et al. (2009). Organic aerosol formation in urban and industrial plumes near Houston and Dallas, Texas. *Journal of Geophysical Research*, *114*, D00F16. https://doi.org/10.1029/2008JD011493

Bond, T. C. (2004). A technology-based global inventory of black and organic carbon emissions from combustion. *Journal of Geophysical Research*, *109*(D14), D14203. https://doi.org/10.1029/2003JD003697

Briggs, N. L., Jaffe, D. A., Gao, H., Hee, J. R., Baylon, P. M., Zhang, Q., et al. (2017). Particulate matter, ozone, and nitrogen species in aged wildfire plumes observed at the Mount bachelor observatory. *Aerosol and Air Quality Research*, *16*(12), 3075–3087. https://doi.org/10.4209/aaqr.2016.03.0120

Browne, E. C., Perring, A. E., Wooldridge, P. J., Apel, E., Hall, S. R., Huey, L. G., et al. (2011). Global and regional effects of the photochemistry of $CH_3 O_2 NO_2$: Evidence from ARCTAS. *Atmospheric Chemistry and Physics*, *11*(9), 4209–4219. https://doi.org/10.5194/acp-11-4209-2011

Burling, I. R., Yokelson, R. J., Griffith, D. W. T., Johnson, T. J., Veres, P., Roberts, J. M., et al. (2010). Laboratory measurements of trace gas emissions from biomass burning of fuel types from the southeastern and southwestern United States. *Atmospheric Chemistry and Physics*, *10*(22), 11115–11130. https://doi.org/10.5194/acp-10-11115-2010

Cai, C., Kulkarni, S., Zhao, Z., Kaduwela, A. P., Avise, J. C., DaMassa, J. A., et al. (2016). Simulating reactive nitrogen, carbon monoxide, and ozone in California during ARCTAS-CARB 2008 with high wildfire activity. *Atmospheric Environment*, *128*, 28–44. https://doi.org/10.1016/j.atmosenv.2015.12.031

Coggon, M. M., Veres, P. R., Yuan, B., Koss, A., Warneke, C., Gilman, J. B., et al. (2016). Emissions of nitrogen-containing organic compounds from the burning of herbaceous and arboraceous biomass: Fuel composition dependence and the variability of commonly used nitrile tracers. *Geophysical Research Letters*, *43*(18), 9903–9912. https://doi.org/10.1002/2016GL070562

Crutzen, P. J., & Andreae, M. O. (1990). Biomass Burning in the Tropics: Impact on Atmospheric Chemistry and Biogeochemical Cycles. *Science*, *250*(4988), 1669–1678. https://doi.org/10.1126/science.250.4988.1669

DeCarlo, P. F., Kimmel, J. R., Trimborn, A., Northway, M. J., Jayne, J. T., Aiken, A. C., et al. (2006). Field-deployable, high-resolution, time-of-flight aerosol mass spectrometer. *Analytical Chemistry*, *78*(24), 8281–8289. https://doi.org/10.1021/ac061249n

Farmer, D. K., Matsunaga, A., Docherty, K. S., Surratt, J. D., Seinfeld, J. H., Ziemann, P. J., et al. (2010). Response of an aerosol mass spectrometer to organonitrates and organosulfates and implications for atmospheric chemistry. *Proceedings of the National Academy of Sciences*, *107*(15), 6670–6675. https://doi.org/10.1073/pnas.0912340107

Fearnside, P. M., Leal, N., & Fernandes, F. M. (1993). Rainforest burning and the global carbon budget: Biomass, combustion efficiency, and charcoal formation in the Brazilian Amazon. *Journal of Geophysical Research: Atmospheres*, *98*(D9), 16733. https://doi.org/10.1029/93JD01140

Finewax, Z., de Gouw, J. A., & Ziemann, P. J. (2018). Identification and quantification of 4-Nitrocatechol formed from OH and NO_3 radical-initiated reactions of catechol in air in the presence of NO_x: Implications for secondary organic aerosol formation from biomass burning. *Environmental Science & Technology*, *52*(4), 1981–1989. https://doi.org/10.1021/acs.est.7b05864

Garofalo, L. A., Pothier, M. A., Levin, E. J. T., Campos, T., Kreidenweis, S. M., & Farmer, D. K. (2019). Emission and evolution of submicron organic aerosol in smoke from wildfires in the Western United States. *ACS Earth and Space Chemistry*, *3*(7), 1237–1247. https://doi.org/10.1021/acsearthspacechem.9b00125

Gilman, J. B., Lerner, B. M., Kuster, W. C., Goldan, P. D., Warneke, C., Veres, P. R., et al. (2015). Biomass burning emissions and potential air quality impacts of volatile organic compounds and other trace gases from fuels common in the US. *Atmospheric Chemistry and Physics*, *15*(24), 13915–13938. https://doi.org/10.5194/acp-15-13915-2015

Glarborg, P., Miller, J. A., Ruscic, B., & Klippenstein, S. J. (2018). Modeling nitrogen chemistry in combustion. *Progress in Energy and Combustion Science*, *67*, 31–68. https://doi.org/10.1016/j.pecs.2018.01.002

Goode, J. G., Yokelson, R. J., Ward, D. E., Susott, R. A., Babbitt, R. E., Davies, M. A., et al. (2000). Measurements of excess O_3, CO_2, CO, CH_4, C_2H_4, C_2H_2, HCN, NO, NH_3, HCOOH, CH_3 COOH, HCHO, and CH_3 OH in 1997 Alaskan biomass burning plumes by airborne Fourier transform infrared spectroscopy (AFTIR). *Journal of Geophysical Research*, *105*(D17), 22147–22166. https://doi.org/10.1029/2000JD900287

Hansson, K.-M., Samuelsson, J., Tullin, C., & Åmand, L.-E. (2004). Formation of HNCO, HCN, and NH_3 from the pyrolysis of bark and nitrogen-containing model compounds. *Combustion and Flame*, *137*(3), 265–277. https://doi.org/10.1016/j.combustflame.2004.01.005

Hatch, L. E., Luo, W., Pankow, J. F., Yokelson, R. J., Stockwell, C. E., & Barsanti, K. C. (2015). Identification and quantification of gaseous organic compounds emitted from biomass burning using two-dimensional gas chromatography–time-of-flight mass spectrometry. *Atmospheric Chemistry and Physics*, *15*(4), 1865–1899. https://doi.org/10.5194/acp-15-1865-2015

Hobbs, P. V., Sinha, P., Yokelson, R. J., Christian, T. J., Blake, D. R., Gao, S., et al. (2003). Evolution of gases and particles from a savanna fire in South Africa. *Journal of Geophysical Research*, *108*(D13). https://doi.org/10.1029/2002JD002352

Holloway, T., Levy, H., & Kasibhatla, P. (2000). Global distribution of carbon monoxide. *Journal of Geophysical Research*, *105*(D10), 12123–12147. https://doi.org/10.1029/1999JD901173

Hudman, R. C., Jacob, D. J., Cooper, O. R., Evans, M. J., Heald, C. L., Park, R. J., et al. (2004). Ozone production in transpacific Asian pollution plumes and implications for ozone air quality in California. *Journal of Geophysical Research*, *109*(D23). https://doi.org/10.1029/2004JD004974

Jacob, D. J., Crawford, J. H., Maring, H., Clarke, A. D., Dibb, J. E., Emmons, L. K., et al. (2010). The Arctic research of the composition of the troposphere from aircraft and satellites (ARCTAS) mission: Design, execution, and first results. *Atmospheric Chemistry and Physics*, *10*(11), 5191–5212. https://doi.org/10.5194/acp-10-5191-2010

Jacob, D. J., Wofsy, S. C., Bakwin, P. S., Fan, S.-M., Harriss, R. C., Talbot, R. W., et al. (1992). Summertime photochemistry of the troposphere at high northern latitudes. *Journal of Geophysical Research*, *97*(D15), 16421. https://doi.org/10.1029/91JD01968

Keywood, M., Kanakidou, M., Stohl, A., Dentener, F., Grassi, G., Meyer, C. P., et al. (2013). Fire in the air: Biomass burning impacts in a changing climate. *Critical Reviews in Environmental Science and Technology*, *43*(1), 40–83. https://doi.org/10.1080/10643389.2011.604248

Kind, I., Berndt, T., Böge, O., & Rolle, W. (1996). Gas-phase rate constants for the reaction of NO3 radicals with furan and methyl-substituted furans. *Chemical Physics Letters*, *256*(6), 679–683. https://doi.org/10.1016/0009-2614(96)00513-1

Kleinman, L. I., Sedlacek, A. J., III, Adachi, K., Buseck, P. R., Collier, S., Dubey, M. K., et al. (2020). Rapid evolution of aerosol particles and their optical properties downwind of wildfires in the Western U.S. *Atmospheric Chemistry and Physics*, *20*, 13319–13341. https://doi.org/10.5194/acp-2020-239

Koss, A. R., Sekimoto, K., Gilman, J. B., Selimovic, V., Coggon, M. M., Zarzana, K. J., et al. (2018). Non-methane organic gas emissions from biomass burning: Identification, quantification, and emission factors from PTR-ToF during the FIREX 2016 laboratory experiment. *Atmospheric Chemistry and Physics*, *18*(5), 3299–3319. https://doi.org/10.5194/acp-18-3299-2018

Kuhlbusch, T. A., Lobert, J. M., Crutzen, P. J., & Warneck, P. (1991). Molecular nitrogen emissions from denitrification during biomass burning. *Nature*, *351*(6322), 135–137. https://doi.org/10.1038/351135a0

Lebegue, B., Schmidt, M., Ramonet, M., Wastine, B., Yver Kwok, C., Laurent, O., et al. (2016). Comparison of nitrous oxide (N_2 O) analyzers for high-precision measurements of atmospheric mole fractions. *Atmospheric Measurement Techniques*, *9*(3), 1221–1238. https://doi.org/10.5194/amt-9-1221-2016

Lee, B. H., Lopez-Hilfiker, F. D., Mohr, C., Kurtén, T., Worsnop, D. R., & Thornton, J. A. (2014). An iodide-adduct high-resolution time-of-flight chemical-ionization mass spectrometer: Application to atmospheric inorganic and organic compounds. *Environmental Science & Technology*, *48*(11), 6309–6317. https://doi.org/10.1021/es500362a

Lee, B. H., Lopez-Hilfiker, F. D., Veres, P. R., McDuffie, E. E., Fibiger, D. L., Sparks, T. L., et al. (2018). Flight deployment of a high-resolution time-of-flight chemical ionization mass spectrometer: Observations of reactive halogen and nitrogen oxide species. *Journal of Geophysical Research: Atmospheres*, *123*, 7670–7686. https://doi.org/10.1029/2017JD028082

Lee, B. H., Mohr, C., Lopez-Hilfiker, F. D., Lutz, A., Hallquist, M., Lee, L., et al. (2016). Highly functionalized organic nitrates in the southeast United States: Contribution to secondary organic aerosol and reactive nitrogen budgets. *Proceedings of the National Academy of Sciences*, *113*(6), 1516–1521. https://doi.org/10.1073/pnas.1508108113

Lindaas, J., Farmer, D. K., Pollack, I. B., Abeleira, A., Flocke, F., Roscioli, R., et al. (2017). The impact of aged wildfire smoke on atmospheric composition and ozone in the Colorado Front Range in summer 2015. *Atmospheric Chemistry and Physics*, *17*, 10691–10707. https://doi.org/10.5194/acp-17-10691-2017

Lindaas, J., Pollack, I. B., Calahorrano, J. J., O'Dell, K., Garofalo, L. A., Pothier, M. A., et al. Empirical insights into the fate of ammonia in western U.S. wildfire smoke plumes. *(in review at journal of Geophysical research: Atmospheres)*.

Lindaas, J., Pollack, I. B., Garofalo, L. A., Pothier, M. A., Farmer, D. K., Kreidenweis, S. M., et al. (2020). Emissions of reactive nitrogen from Western U.S. wildfires during Summer 2018. *Journal of Geophysical Research: Atmospheres*, e2020JD032657. https://doi.org/10.1029/2020JD032657

Liu, X., Huey, L. G., Yokelson, R. J., Selimovic, V., Simpson, I. J., Müller, M., et al. (2017). Airborne measurements of western U.S. wildfire emissions: Comparison with prescribed burning and air quality implications. *Journal of Geophysical Research: Atmospheres*, *122*(11), 6108–6129. https://doi.org/10.1002/2016JD026315

Liu, X., Zhang, Y., Huey, L. G., Yokelson, R. J., Wang, Y., Jimenez, J. L., et al. (2016). Agricultural fires in the southeastern U.S. during SEAC^4 RS: Emissions of trace gases and particles and evolution of ozone, reactive nitrogen, and organic aerosol. *Journal of Geophysical Research: Atmospheres*, *121*(12), 7383–7414. https://doi.org/10.1002/2016JD025040

Lobert, J. M., Scharffe, D. H., Hao, W. M., & Crutzen, P. J. (1990). Importance of biomass burning in the atmospheric budgets of nitrogen-containing gases. *Nature*, *346*(6284), 552–554. https://doi.org/10.1038/346552a0

Matsumoto, K., & Tanaka, H. (1996). Formation and dissociation of atmospheric particulate nitrate and chloride: An approach based on phase equilibrium. *Atmospheric Environment*, *30*(4), 639–648. https://doi.org/10.1016/1352-2310(95)00290-1

McMeeking, G. R., Kreidenweis, S. M., Baker, S., Carrico, C. M., Chow, J. C., Collett, J. L., et al. (2009). Emissions of trace gases and aerosols during the open combustion of biomass in the laboratory. *Journal of Geophysical Research*, *114*(D19), D19210. https://doi.org/10.1029/2009JD011836

Moritz, M. A., Parisien, M.-A., Batllori, E., Krawchuk, M. A., Van Dorn, J., Ganz, D. J., et al. (2012). Climate change and disruptions to global fire activity. *Ecosphere*, *3*(6), 1–22. https://doi.org/10.1890/ES11-00345.1

O'Dell, K., Hornbrook, R. S., Permar, W., Levin, E. J. T., Garofalo, L. A., Apel, E. C., et al. (2020). *Hazardous air pollutants in fresh and aged Western US Wildfire smoke and implications for long-term exposure.* Environmental Science & Technology. https://doi.org/10.1021/acs.est.0c04497

Palm, B. B., Liu, X., Jimenez, J. L., & Thornton, J. A. (2019). Performance of a new coaxial ion–molecule reaction region for low-pressure chemical ionization mass spectrometry with reduced instrument wall interactions. *Atmospheric Measurement Techniques*, *12*(11), 5829–5844. https://doi.org/10.5194/amt-12-5829-2019

Peng, Q., Palm, B. B., Melander, K. E., Lee, B. H., Hall, S. R., Ullmann, K., et al. (2020). HONO emissions from Western U.S. wildfires provide dominant radical source in fresh wildfire smoke. *Environmental Science & Technology*, *54*(10), 5954–5963. https://doi.org/10.1021/acs.est.0c00126

Ren, Q., & Zhao, C. (2012). NO$_x$ and N$_2$O precursors from biomass pyrolysis: Nitrogen transformation from amino acid. *Environmental Science & Technology*, *46*(7), 4236–4240. https://doi.org/10.1021/es204142e

Ridley, B. A., & Grahek, F. E. (1990). A small, low flow, high sensitivity reaction vessel for NO/O3 chemiluminescence detectors. *Journal of Atmospheric and Oceanic Technology*, *7*, 307–311. https://doi.org/10.1175/1520-0426(1990)007<0307:ASLFHS>2.0.CO;2

Roberts, J. M., Stockwell, C. E., Yokelson, R. J., de Gouw, J., Liu, Y., Selimovic, V., et al. (2020). The nitrogen budget of laboratory-simulated western U.S. wildfires during the FIREX 2016 FireLab study. *Atmospheric Chemistry and Physics*, *20*, 8807–8826.

Scharko, N. K., Oeck, A. M., Myers, T. L., Tonkyn, R. G., Banach, C. A., Baker, S. P., et al. (2019). Gas-phase pyrolysis products emitted by prescribed fires in pine forests with a shrub understory in the southeastern United States. *Atmospheric Chemistry and Physics*, *19*(15), 9681–9698. https://doi.org/10.5194/acp-19-9681-2019

Scholze, M., Knorr, W., Arnell, N. W., & Prentice, I. C. (2006). A climate-change risk analysis for world ecosystems. *Proceedings of the National Academy of Sciences*, *103*(35), 13116–13120. https://doi.org/10.1073/pnas.0601816103

Seinfeld, J. H., & Pandis, S. N. (2006). *Atmospheric chemistry and physics: From air pollution to climate change.* Hoboken, NJ: J. Wiley.

Sekimoto, K., Li, S.-M., Yuan, B., Koss, A., Coggon, M., Warneke, C., et al. (2017). Calculation of the sensitivity of proton-transfer-reaction mass spectrometry (PTR-MS) for organic trace gases using molecular properties. *International Journal of Mass Spectrometry*, *421*, 71–94. https://doi.org/10.1016/j.ijms.2017.04.006

Selimovic, V., Yokelson, R. J., McMeeking, G. R., & Coefield, S. (2020). Aerosol mass and optical properties, smoke influence on O$_3$, and high NO$_3$ production rates in a Western U.S. city impacted by wildfires. *Journal of Geophysical Research: Atmospheres*, *125*(16). https://doi.org/10.1029/2020JD032791

Selimovic, V., Yokelson, R. J., Warneke, C., Roberts, J. M., de Gouw, J., Reardon, J., et al. (2018). Aerosol optical properties and trace gas emissions by PAX and OP-FTIR for laboratory-simulated western US wildfires during FIREX. *Atmospheric Chemistry and Physics*, *18*(4), 2929–2948. https://doi.org/10.5194/acp-18-2929-2018

Shetter, R. E., & Müller, M. (1999). Photolysis frequency measurements using actinic flux spectroradiometry during the PEM-Tropics mission: Instrumentation description and some results. *Journal of Geophysical Research*, *104*(D5), 5647–5661. https://doi.org/10.1029/98JD01381

Singh, H. B. (1987). Reactive nitrogen in the troposphere. *Environmental Science & Technology*, *21*(4), 320–327. https://doi.org/10.1021/es00158a001

Singh, H. B., Anderson, B. E., Brune, W. H., Cai, C., Cohen, R. C., Crawford, J. H., et al. (2010). Pollution influences on atmospheric composition and chemistry at high northern latitudes: Boreal and California forest fire emissions. *Atmospheric Environment*, *44*(36), 4553–4564. https://doi.org/10.1016/j.atmosenv.2010.08.026

Singh, H. B., Cai, C., Kaduwela, A., Weinheimer, A., & Wisthaler, A. (2012). Interactions of fire emissions and urban pollution over California: Ozone formation and air quality simulations. *Atmospheric Environment*, *56*, 45–51. https://doi.org/10.1016/j.atmosenv.2012.03.046

Slusher, D. L., Huey, L. G., Tanner, D. J., Flocke, F. M., & Roberts, J. M. (2004). A thermal dissociation–chemical ionization mass spectrometry (TD-CIMS) technique for the simultaneous measurement of peroxyacyl nitrates and dinitrogen pentoxide. *Journal of Geophysical Research*, *109*(D19), D19315. https://doi.org/10.1029/2004JD004670

Stelson, A., & Seinfeld, J. (1982). Relative humidity and temperature dependence of the ammonium nitrate dissociation constant. *Atmospheric Environment*, *16*, 983–992. https://doi.org/10.1016/j.atmosenv.2007.10.063

Stockwell, C. E., Veres, P. R., Williams, J., & Yokelson, R. J. (2015). Characterization of biomass burning emissions from cooking fires, peat, crop residue, and other fuels with high-resolution proton-transfer-reaction time-of-flight mass spectrometry. *Atmospheric Chemistry and Physics*, *15*(2), 845–865. https://doi.org/10.5194/acp-15-845-2015

Tabazadeh, A., Jacobson, M. Z., Singh, H. B., Toon, O. B., Lin, J. S., Chatfield, R. B., et al. (1998). Nitric acid scavenging by mineral and biomass burning aerosols. *Geophysical Research Letters*, *25*(22), 4185–4188. https://doi.org/10.1029/1998GL900062

Trentmann, J., Yokelson, R. J., Hobbs, P. V., Winterrath, T., Christian, T. J., Andreae, M. O., et al. (2005). An analysis of the chemical processes in the smoke plume from a savanna fire. *Journal of Geophysical Research*, *110*(D12), D12301. https://doi.org/10.1029/2004JD005628

Val Martín, M., Honrath, R. E., Owen, R. C., Pfister, G., Fialho, P., & Barata, F. (2006). Significant enhancements of nitrogen oxides, black carbon, and ozone in the North Atlantic lower free troposphere resulting from North American boreal wildfires. *Journal of Geophysical Research*, *111*(D23). https://doi.org/10.1029/2006JD007530

Westerling, A. L. (2016). Increasing western US forest wildfire activity: Sensitivity to changes in the timing of spring. *Philosophical Transactions of the Royal Society B: Biological Sciences*, *371*(1696), 20150178. https://doi.org/10.1098/rstb.2015.0178

Williams, A. P., Abatzoglou, J. T., Gershunov, A., Guzman-Morales, J., Bishop, D. A., Balch, J. K., et al. (2019). Observed impacts of anthropogenic climate change on Wildfire in California. *Earth's Future*, *7*(8), 892–910. https://doi.org/10.1029/2019EF001210

Wu, H., Taylor, J. W., Szpek, K., Langridge, J., Williams, P. I., Flynn, M., et al. (2020). Vertical variability of the properties of highly aged biomass burning aerosol transported over the southeast Atlantic during CLARIFY-2017. *Atmospheric Chemistry and Physics*. https://doi.org/10.5194/acp-2020-197

Xiang, B., Patra, P. K., Montzka, S. A., Miller, S. M., Elkins, J. W., Moore, F. L., et al. (2014). Global emissions of refrigerants HCFC-22 and HFC-134a: Unforeseen seasonal contributions. *Proceedings of the National Academy of Sciences*, *111*(49), 17379–17384. https://doi.org/10.1073/pnas.1417372111

Yokelson, R. J., Crounse, J. D., DeCarlo, P. F., Karl, T., Urbanski, S., Atlas, E., et al. (2009). Emissions from biomass burning in the Yucatan. *Atmospheric Chemistry and Physics*, *9*, 5785–8512. https://doi.org/10.5194/acp-9-5785-2009

Yokelson, R. J., Griffith, D. W. T., & Ward, D. E. (1996). Open-path Fourier transform infrared studies of large-scale laboratory biomass fires. *Journal of Geophysical Research*, *101*(D15), 21067–21080. https://doi.org/10.1029/96JD01800

Yuan, B., Koss, A. R., Warneke, C., Coggon, M., Sekimoto, K., & de Gouw, J. A. (2017). Proton-transfer-reaction mass spectrometry: Applications in atmospheric sciences. *Chemical Reviews*, *117*(21), 13187–13229. https://doi.org/10.1021/acs.chemrev.7b00325

Yue, X., Mickley, L. J., Logan, J. A., & Kaplan, J. O. (2013). Ensemble projections of wildfire activity and carbonaceous aerosol concentrations over the western United States in the mid-21st century. *Atmospheric Environment*, *77*, 767–780. https://doi.org/10.1016/j.atmosenv.2013.06.003

Zheng, W., Flocke, F. M., Tyndall, G. S., Swanson, A., Orlando, J. J., Roberts, J. M., et al. (2011). Characterization of a thermal decomposition chemical ionization mass spectrometer for the measurement of peroxy acyl nitrates (PANs) in the atmosphere. *Atmospheric Chemistry and Physics*, *11*, 6529–6547. https://doi.org/10.5194/acp-11-6529-2011